Journal of Materials Chemistry A

ROYAL SOCIETY OF CHEMISTRY

PAPER

View Article Online
View Journal | View Issue

Check for updates

Cite this: J. Mater. Chem. A, 2025, 13, 32271

In situ studies of oxygen transport mechanisms in Ag/$SrFeO_{3-\delta}$ materials for chemical looping catalysis

Alexander R. P. Harrison, *[ab] Felix Donat, [c] James M. A. Steele, [de] Joseph C. Gebers, [a] Simon M. Fairclough, [f] Elizabeth A. Willneff,[gh] Andrew J. Britton,[gh] Christopher L. Truscott,[d] Christoph R. Müller, [c] Caterina Ducati, [f] Clare P. Grey [d] and Ewa J. Marek *[a]

Strontium ferrite ($SrFeO_{3-\delta}$) impregnated with a noble metal (*e.g.* Ag) has been applied to catalyse selective oxidation reactions in a chemical looping mode, such as in ethylene epoxidation or ethanol dehydrogenation. The metal oxide donates oxygen to the reaction at the Ag catalyst, and then is re-oxidised in air in a separate step, however the mechanisms of oxygen transport are poorly understood. Here, we investigated the transport of oxygen within Ag/$SrFeO_{3-\delta}$ materials *in situ* to determine the mechanisms by which Ag improves the redox activity of $SrFeO_{3-\delta}$. X-ray diffraction under 5 vol% H_2 showed that the Ag nanoparticles decreased the temperature required for phase transformation from perovskite to brownmillerite structure, $SrFeO_{2.5}$, from *c.* 500 °C for bare $SrFeO_{3-\delta}$ to *c.* 300 °C for Ag/$SrFeO_{3-\delta}$. Near-ambient pressure X-ray photoelectron spectroscopy (NAP-XPS) and Raman spectroscopy showed that Ag–O_x surface intermediates enhance the release and uptake of oxygen, confirming that Ag takes an active role in the reduction of Ag/$SrFeO_{3-\delta}$.

Received 18th June 2025
Accepted 22nd August 2025

DOI: 10.1039/d5ta04944j

rsc.li/materials-a

Open Access Article. Published on 26 August 2025. Downloaded on 2/23/2026 2:45:46 PM. This article is licensed under a Creative Commons Attribution 3.0 Unported Licence.

1 Introduction

Silver-strontium ferrite composites have been investigated for catalytic selective oxidation processes in a chemical looping mode, including epoxidation of ethylene[1–3] and dehydrogenation of ethanol to acetaldehyde,[4] whereby oxygen is supplied from the lattice of the metal oxide support (termed an 'oxygen carrier') to the active site of Ag, and subsequently re-oxidised in air. Under strong reducing conditions, such as H_2 or CO at ≥500 °C, $SrFeO_{3-\delta}$ undergoes a reversible phase change to brownmillerite $SrFeO_{2.5}$.[5] Further reduction to *e.g.* SrO and Fe allows for chemical looping processes at very low oxidising potential, such as conversion of CO_2 to CO[5] or hydrogen production *via* thermo-chemical splitting of H_2O.[6]

In our previous work,[7] the addition of Ag nanoparticles to $SrFeO_{3-\delta}$ aided the removal of oxygen from the oxide lattice, and increased the rate of release of O_2 gas from the solid, termed 'oxygen uncoupling', under relatively mild conditions (reduction in N_2 and re-oxidation in air, 475–600 °C). The presence of Ag nanoparticles at the surface of $SrFeO_{3-\delta}$ has been found to facilitate transport of oxygen by withdrawing electron density from the perovskite, aiding the formation of oxygen vacancies.[8,9] Silver also catalyses reactions between oxygen surface species to facilitate formation and dissociation of O_2.[10–12] Additionally, from studies of oxidation of hydrocarbons over $CeO_{2-\delta}$ materials with and without Ag catalysts, the addition of Ag altered the distribution of oxygen surface species detected at the surface (*e.g.* atomic oxygen, peroxide, and superoxide species),[9,13–15] and changed the reaction mechanism from Mars-Van Krevelen (direct reaction between the hydrocarbon with $CeO_{2-\delta}$ lattice oxygen) to Langmuir–Hinshelwood (reaction between the adsorbed hydrocarbon and O_a adatoms at the Ag surface).[16] However, while previous studies have demonstrated that the addition of Ag to $SrFeO_{3-\delta}$ results in faster oxygen removal and uptake, the relative influence of Ag on specific oxygen pathways or the formation of active transient

[a]Department of Chemical Engineering and Biotechnology, University of Cambridge, Philippa Fawcett Drive, Cambridge, CB3 0AS, UK. E-mail: alexander.harrison@eng.ox.ac.uk; ejm94@cam.ac.uk; jcg71@cam.ac.uk

[b]Department of Engineering Science, University of Oxford, Parks Road, Oxford, OX1 3PJ, UK

[c]Department of Mechanical and Process Engineering, ETH Zürich, Leonhardstrasse 21, Zürich, CH-8092, Switzerland. E-mail: donatf@ethz.ch; muelchri@ethz.ch

[d]Yusuf Hamied Department of Chemistry, University of Cambridge, Lensfield Road, Cambridge, CB2 1EW, UK. E-mail: jmas5@cam.ac.uk; clt45@cam.ac.uk; cpg27@cam.ac.uk

[e]Maxwell Centre, Cavendish Laboratory, University of Cambridge, JJ Thomson Ave, Cambridge, CB3 0HE, UK

[f]Department of Materials Science and Metallurgy, University of Cambridge, 27 Charles Babbage Road, Cambridge, CB3 0FS, UK. E-mail: smf57@cam.ac.uk; cd251@cam.ac.uk

[g]Versatile X-ray Spectroscopy Facility, University of Leeds, 211 Clarendon Road, Leeds, LS2 9JT, UK. E-mail: eawillneff@gmail.com; A.Britton@leeds.ac.uk

[h]Faculty of Engineering and Physical Sciences, University of Leeds, 211 Clarendon Road, Leeds, LS2 9JT, UK

Open Access Article. Published on 26 August 2025. Downloaded on 2/23/2026 2:45:46 PM. This article is licensed under a Creative Commons Attribution 3.0 Unported Licence.

species remains unclear. Indeed, the question remains whether Ag promotes alternative catalytic pathways *via* formation of Ag–O surface oxygen species, or, aids oxygen availability from the bulk oxide lattice by improving oxygen ion mobility, as speculated in a few preliminary studies.[2]

Moreover, while previous literature has investigated the role of Ag in surface reactions, the pathways taken by oxygen from the bulk of the $SrFeO_{3-\delta}$ to form the oxygen surface species on Ag have yet to be determined. In this work, the bulk and surface properties of $SrFeO_{3-\delta}$ impregnated with nanoparticles of Ag were investigated during reduction and oxidation, in order to elucidate the mechanisms of oxygen release and re-uptake. The influence of Ag on the phase stability of $SrFeO_{3-\delta}$ was investigated using *in situ* XRD under reducing and oxidising atmospheres, while the spatial variation in oxygen content under reduction was assessed with TEM. Then, XPS, Raman spectroscopy, and temperature programmed reduction in H_2 were applied to probe the species present at the surface of $SrFeO_{3-\delta}$ and Ag/$SrFeO_{3-\delta}$ during reduction and oxidation in H_2 and air, respectively. During reduction at a given temperature and gas environment, the distribution of oxygen species at the surface of the materials under investigation was expected to reach a pseudo-steady state, as surface oxygen species react with hydrogen, and are replenished by oxygen from the $SrFeO_{3-\delta}$ lattice.[17] Applying a temperature ramp under reducing conditions, the changes in relative abundance of different surface species detected by *in situ* spectroscopy gave an indication of the mechanisms of oxygen transport between the $SrFeO_{3-\delta}$ support and the surface of Ag.

2 Methods

2.1 Synthesis of materials

Strontium ferrite ($SrFeO_{3-\delta}$, written as SFO for brevity) oxygen carriers were prepared *via* a solid state method.[5,7] Stoichiometric amounts of Fe_2O_3 (0.25 mol, Honeywell Fluka, >99%) and $SrCO_3$ (0.5 mol, Sigma Aldrich, 98%) were thoroughly mixed, then, 75 mL ethanol (Fisher Scientific, HPLC grade) was added as a binder. The mixture was milled using a ball mill (Pulverisette 6, Fritsch) with stainless steel balls and grinding jar, with 2 min of milling at 600 rpm, followed by 20 min of cooling between milling steps, repeated 15 times. The resulting paste was dried in static air for 24 h at 50 °C crushed and sieved to <355 μm. The resulting particles were calcined in two steps of 4 h and 18 h at 1000 °C under static air in an electric muffle furnace (Carbolite), with intermediate cooling to room temperature, then sieved to 180–355 μm. The initial stoichiometry of the prepared material was shown previously[7] to be $SrFeO_{2.82}$. Particles of Ag were deposited onto SFO by incipient wetness impregnation, referred to as Ag/SFO. Silver nitrate solution was prepared by dissolving $AgNO_3$ (Alfa Aesar, >99.8%) in DI water, then, added dropwise to SFO (180–355 μm) in a single step, with manual mixing between addition of drops of solution. The volume of water used was selected to approximately equal the volume of macropores in the SFO, estimated by adding water dropwise to a sample of SFO until the particles cohered. The impregnated particles were then dried at 120 °C for 12 h, and calcined at 650 °C in an electric muffle furnace under static air for 5 h to decompose the nitrate species, leaving 10 wt% metallic Ag at the surface of the SFO. A sample of Ag/SFO with a higher loading of 15 wt% Ag was prepared for *in situ* transmission electron microscopy (TEM), to facilitate finding suitable particles of Ag on the sample. For use in XPS and Raman spectroscopy analysis, samples of SFO and Ag/SFO were compressed to form flat pellets, of diameter 7 or 13 mm.

2.2 *In situ* X-ray diffraction (XRD)

Powder X-ray diffraction (XRD) measurements were collected using a Malvern Panalytical Empyrean diffractometer. Measurements were collected over the angular range $2\theta = 20$–80°, with step resolution 0.02° and step time 2 s, using Cu Kα radiation (1.5418 Å). For *in situ* measurements at elevated temperature (200–800 °C) and under variable atmospheres, a heated stage (Anton Paar XRK 900) was used, with gases (compressed air, N_2, and 5 vol% H_2 in N_2, all BOC or Carbagas) delivered at a flowrate of 200 mL min^{-1}, and two successive scans collected at each temperature. Rietveld refinement was performed using TOPAS software,[18] using reference patterns for fitted phases from the ICSD database[19] (ICSD collection codes are given in the (SI), Table S1).

2.3 *In situ* transmission electron microscopy (TEM)

Samples were prepared for *in situ* TEM analysis by manually crushing particles of SFO and Ag/SFO in an agate mortar. The resulting powder was then suspended in $CHCl_3$ (Sigma Aldrich, >99%), and a drop of the resulting suspension was deposited onto a heating chip (DENSSolutions Wildfire, shown in the SI, Fig. S1), and dried for 45 min at 50 °C. The TEM measurements were performed using a Thermo Fisher Scientific Spectra 300 TEM operating at 300 kV accelerating voltage. The sample chamber was evacuated to 10^{-8} mbar total pressure, corresponding to an oxygen partial pressure of approximately $pO_2 = 2.1 \times 10^{-7}$ Pa.

Selected area electron diffraction (SAED) patterns were collected at each point on the sample using a MerlinEM direct electron detector (Quantum Detectors), alongside energy dispersive X-ray spectroscopy (EDS) and electron energy loss spectroscopy (EELS) measurements, collected using SuperX EDS (Thermo Fisher Scientific) and Continuum EELS (Gatan) detectors respectively. The resulting EDS and EELS spectra were processed and analysed using the Hyperspy Python package[20] as described in the SI, Sections S1.1 and S1.2.

Reference EELS measurements of iron compounds with known oxidation state[21] were used to correlate the intensity of Fe-L_3 and Fe-L_2 peaks in the EELS spectra to the local oxidation state of Fe in the sample.[22,23] Simulated SAED patterns were generated using SingleCrystal® (CrystalMaker Software).

For both samples, the sample was heated in a series of temperature steps (20, 200, 400, and 600 °C for SFO; 20, 200, 300, 400, 500, 600 and 700 °C for Ag/SFO). A further set of scans was collected for Ag/SFO after cooling to room temperature. At each temperature, the sample was allowed to settle for 5–10 min, then, EELS and EDS scans were collected in parallel,

 This journal is © The Royal Society of Chemistry 2025

Open Access Article. Published on 26 August 2025. Downloaded on 2/23/2026 2:45:46 PM. This article is licensed under a Creative Commons Attribution 3.0 Unported Licence.

with a total scan time of approximately 10 min, and subsequently images and SAED scans were collected, with an approximate electron dose of 3×10^5 Å^{-2} per scan. The effect of electron dose on measured EELS spectra is reported in the SI, Fig. S8. The sample was held at each temperature for approximately 45 min, and the time taken to heat or cool the sample was under 10 s for all temperature steps.

2.4 Near-ambient pressure X-ray photoelectron spectroscopy (NAP-XPS)

Near-ambient pressure X-ray photoelectron spectroscopy (NAP-XPS) measurements were performed using a SPECS EnviroESCA NAP-XPS spectrometer, with full hardware parameters described elsewhere.[24] Gases (5 vol% H_2 in N_2, N_2, or compressed air, all BOC, 99.99+%) were supplied using mass flow controllers, with composition in the sample chamber measured using a mass spectrometer (MS, MKS e-Vision 2). Pellets of SFO or Ag/SFO (13 mm diameter, *c.* 1 mm thickness) were clamped onto a ceramic button heater, with temperature controlled between 25–430 °C by varying the current supplied through a resistive heating coil. The X-ray beam spot size on the sample was *c.* 0.3 mm in diameter, and the working distance from the nozzle to the sample was *c.* 0.3 mm. Prior to NAP-XPS measurements, samples were cleaned of carbonate species adsorbed at the surface by heating to 650 °C in ambient air for 5 h. The samples were then stored in an Ar-filled glovebox, and transferred to the NAP-XPS instrument immediately before collecting measurements. Any residual carbonate remaining on the sample desorbed upon heating to temperatures above 177 °C, evidenced by the disappearance of the carbonate peak in the C 1s spectrum. During heating, the gas environment was set to 0.25 mbar H_2 by feeding 30 mL min^{-1} 5 vol% H_2 in N_2, and during cooling, to 1 mbar O_2 by feeding 30 mL min^{-1} compressed air. Total pressure in the sample chamber was kept constant at 5 mbar by feeding N_2 as a balance gas, in order to avoid changes in signal attenuation or binding energy induced by changing pressure,[25] with the selected pressure offering a balance of charge compensation at the surface of the sample, signal to noise ratio, and data acquisition time. The monochromated Al K-α X-ray source was operated at 14 kV voltage and 42 W power. Survey scans were collected in 1 sweep with a step size of 1 eV, dwell time of 0.1 s and pass energy of 100 eV. High-resolution narrow scans were collected sequentially for the C 1s, Sr 3p, O 1s, Fe 3p, Sr 3d, N 1s, and Ag 3d regions in 4 sweeps with a step size of 0.1 eV, dwell time of 0.2 s and pass energy of 50 eV with a total scan time of *c.* 45 min. For the sample of Ag/SFO, scans of the S 2p region were also collected with the same parameters, as sulphur was detected in the survey scan. Furthermore, for Ag/SFO, immediately after the gas switch from H_2 to O_2, successive rapid scans of the O 1s region (523–543 eV, 0.1 eV step size, pass energy of 50 eV and 0.1 seconds of dwell time of total duration 20 s) were collected for 20 min.

Analysis of XPS measurements was performed using CasaXPS software,[26] with a Shirley type background fitted to all regions[27] and all peaks fitted with a Lorentzian asymmetric lineshape. Energy calibration was performed relative to the adventitious carbon C 1s peak (C_{adv}) at 284.8 eV,[28] with the caveat that for measurements at high temperatures (>300 °C) under oxidising conditions, the C_{adv} peak intensity was low, as a result of the carbon desorbing. For NAP-XPS measurements without a clear C_{adv} peak, measurements were calibrated relative to the central position of the Sr $3p_{3/2}$ peak, at 268.4 eV, which was found not to shift substantially (<0.25 eV) with respect to the C_{adv} peak in spectra where both were visible, under variable temperatures and gas atmospheres. The parameters for the binding energies and FWHM of the fitted peaks are given in the SI, Table S3.

2.5 Temperature programmed reduction (H_2-TPR)

Temperature programmed reduction in hydrogen (H_2-TPR) was performed using a Micromeritics AutoChem 2920 II instrument. Samples (*c.* 30 mg, 180–355 μm) of SFO and Ag/SFO were inserted into a quartz U-tube reactor (i.d. 8 mm), and a thermocouple was positioned in the centre of the bed of active material, to record the temperature at the sample. The material was then heated under flow of 5 vol% O_2 (balance He, 20 mL min^{-1}, Carbagas) at 650 °C for 2 h prior to measurements, then cooled to 50 °C, to remove surface impurities. The flowing gas was then switched to 5 vol% H_2 (balance Ar, 20 mL min^{-1}, Carbagas), and the samples were ramped from 50–700 °C at a rate of 5 °C min^{-1}. Hydrogen consumption was measured using an on-line thermal conductivity detector, and the fractions of other gaseous species (H_2O, O_2, CO_2), were measured using an on-line mass spectrometer (MKS Cirrus 2).

2.6 *In situ* Raman spectroscopy

Raman spectroscopy measurements were performed using Thermo Scientific DXR 2 and Horiba Jobin-Yvon LabRAM HR Raman spectrometers, fitted with Linkam CCR1000 heated stages for *in situ* measurements. In a typical experiment, Raman spectra were collected over the wavenumber range 150–1800 cm^{-1} or 150–1450 cm^{-1}, at a laser power of 0.5 mW and 15 s acquisition time, using a 532 nm green laser.

Gases (compressed air, N_2, or 5 vol% H_2 in N_2, all BOC or Carbagas, 99.99+%) were supplied to the stage at a total flowrate of 35 mL min^{-1}, set using mass-flow controllers. The set-point of the heated stage was set to the target temperature (200–350 °C) with a nominal ramp rate of 10 °C min^{-1}, and allowed to settle for 5–10 min prior to measurements.

A pelletised sample of Ag/SFO was cleaned at 650 °C in air to remove any surface carbonate impurities from adsorbed CO_2 (with Ag_2CO_3 decomposing at around 230 °C[29]), and to induce reduction of any residual silver(I) oxide and silver (I, III) oxide (each starting to decompose at around 200 °C, with full reduction to metallic Ag at around 450 °C[30]). The cleaned pellet was then mounted into the heated stage. Reference spectra were collected at room temperature in air, then, the gas flowing through the sample stage was set to 5 vol% H_2. The stage temperature was increased from 200–350 °C in 50 °C increments, with three scans collected at each temperature at a scan time of 2.5 min.

Open Access Article. Published on 26 August 2025. Downloaded on 2/23/2026 2:45:46 PM. This article is licensed under a Creative Commons Attribution 3.0 Unported Licence.

Reference spectra at room temperature were also collected for a pellet of unmodified SFO, as-received Ag_2CO_3 (Sigma Aldrich, 99%), a sample of Ag supported on Al_2O_3 (Boud Minerals, 355–425 μm) prepared by incipient wetness impregnation, and a sample of Ag_2O supported on Al_2O_3 (with details of synthesis given in ref. 31).

3 Results

3.1 Characterisation of structural changes

3.1.1 ***In situ*** **X-ray diffraction.** X-ray diffraction patterns for SFO and Ag/SFO heated under 5 vol% H_2 in N_2 from 200–800 °C, then cooled in air back to 200 °C, are presented in Fig. 1a, with estimated phase compositions given in Fig. 1b.

Representative fitted Rietveld refinement patterns and fit profile residuals are given in the SI, Fig. S9 and Table S2, respectively. For SFO, upon heating in 5 vol% H_2, a phase change from perovskite $SrFeO_{3-\delta}$ to brownmillerite $SrFeO_{2.5}$ was observed at 500 °C, in agreement with previous studies.[32,33] No further phase changes, or decomposition of the $SrFeO_{2.5}$ phase, were observed upon heating to 800 °C, in line with ref. 5. Upon switching the gas atmosphere from 5 vol% H_2 in N_2 to air, the SFO rapidly (≤20 min) re-oxidised to cubic perovskite structure.

For the sample of Ag/SFO, reduction of the perovskite $SrFeO_{3-\delta}$ phase to brownmillerite $SrFeO_{2.5}$ occurred at substantially lower temperature, with partial reduction to 22 wt% and 47 wt% over two successive scans at 200 °C (indicated by formation of a peak shoulder at $2\theta = 32°$, circled in Fig. 1a), and reaching full reduction to $SrFeO_{2.5}$ at 300 °C. Such a decrease in temperature was in broad agreement with the findings from thermogravimetric analysis (TGA) measurements

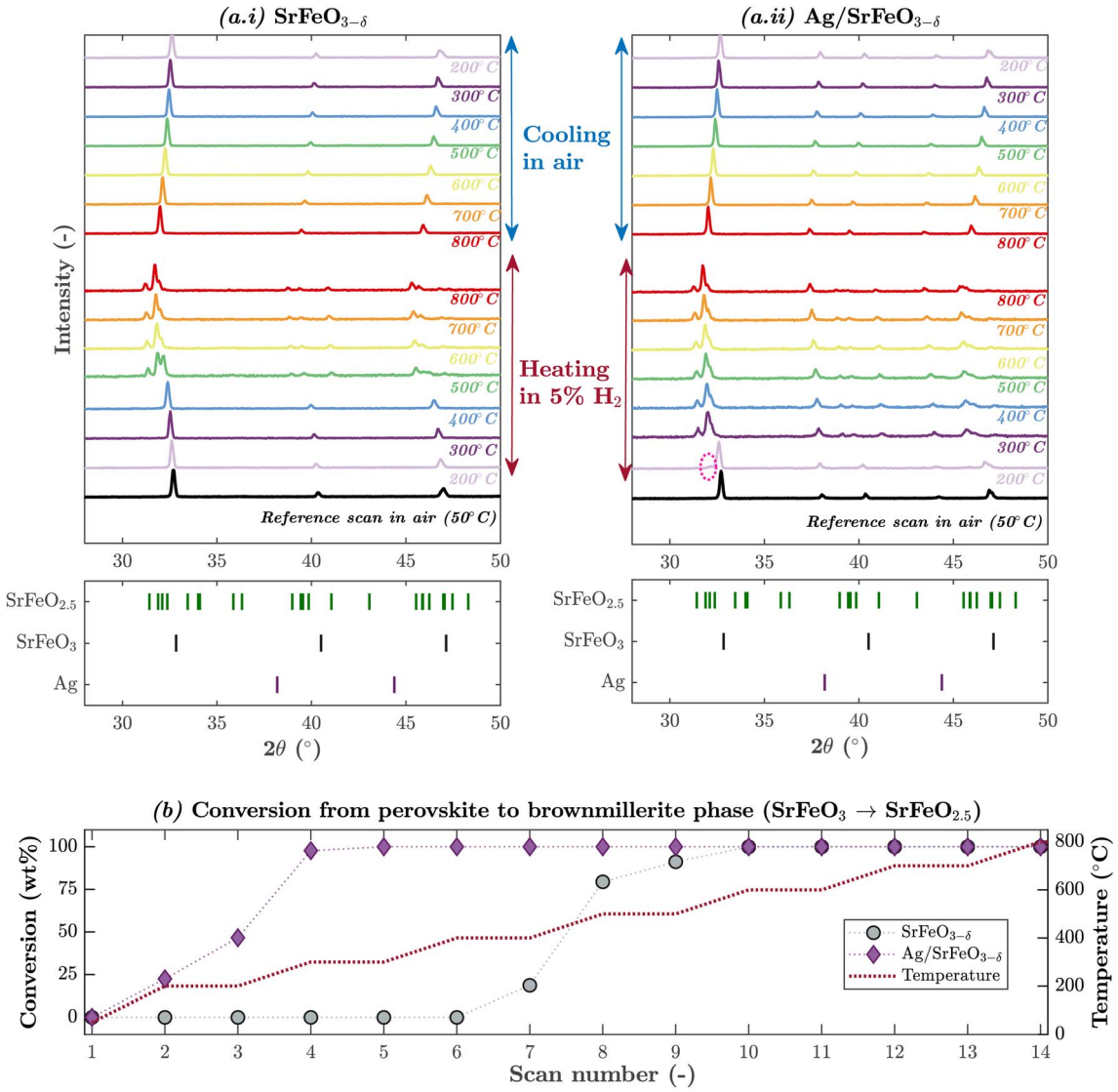

Fig. 1 (a) Sections of *in situ* XRD patterns showing reduction in 5 vol% H_2 and oxidation in air of (i) $SrFeO_{3-\delta}$ and (ii) $Ag/SrFeO_{3-\delta}$, with one scan per temperature shown. Tick markers indicate peak positions in identified phases, circle indicates initial formation of $SrFeO_{2.5}$ phase. (b) Estimated conversion from perovskite to brownmillerite phase over successive scans for each material during reduction in 5 vol% H_2; both samples fully re-oxidised to perovskite form within one scan after switching to air.

 This journal is © The Royal Society of Chemistry 2025

Open Access Article. Published on 26 August 2025. Downloaded on 2/23/2026 2:45:46 PM.
This article is licensed under a Creative Commons Attribution 3.0 Unported Licence.

reported previously,[7] where, under reduction with 5 vol% H_2 in N_2, $SrFeO_{2.5}$ formed at 585 °C for SFO, and at 512 °C for Ag/SFO. The lower temperatures of brownmillerite formation during XRD scans as compared to under TGA are explained by the sample being exposed to 5 vol% H_2 gas directly in the *in situ* XRD stage, whereas, inside the TGA instrument, mixing between the reactive gas and inert purge and protective streams resulted in a lower hydrogen concentration in contact with the sample material (estimated at around 1.67–3.33 vol% H_2).[5,34] The impregnated Ag in Ag/SFO remained as metallic silver throughout the experiment, with no bulk crystalline silver oxide phases detected (Ag_2O or AgO). When the gas was switched to air, as with SFO, the sample rapidly (<20 min) oxidised to re-form the perovskite phase, and after cooling to 200 °C, the XRD measurements overlapped with the results collected for fresh samples.

In situ XRD measurements of SFO and Ag/SFO heated in air from 200–800 °C in 100 °C increments, then, cooled back to 200 °C are shown in the SI, Fig. S10. For both samples, peaks corresponding to the perovskite $SrFeO_3$ phase shifted to lower 2θ values, corresponding to expansion of the crystal lattice.[5,35]

3.1.2 *In situ* transmission electron microscopy. Selected area electron diffraction (SAED) images of Ag/SFO collected at a point near the edge of the sample were compared with simulated patterns for perovskite $SrFeO_3$ ($Pm\bar{3}m$ symmetry[36]) and brownmillerite $SrFeO_{2.5}$ (*Ibm*2 symmetry[37]), shown in Fig. 2. At room temperature, the TEM sample stage was tilted to align the electron beam with the [110] zone axis of a $SrFeO_{3-\delta}$ crystal, allowing the perovskite $SrFeO_3$ and brownmillerite $SrFeO_{2.5}$ phases to be readily distinguishable from their electron diffraction patterns,[38] with the unit cell highlighted in the simulated and measured patterns.

No major changes in the diffraction pattern were observed upon heating up to 500 °C, indicating formation of oxygen vacancies in the perovskite structure without an overall phase change. However, at 600 °C, additional reflections emerged, and became more intense with successive scans (shown in Fig. 2c(vi–viii)), corresponding to formation of a brownmillerite phase aligned along the [221] zone axis, as expected for topotactic phase transition of perovskite to brownmillerite structure.[38] Additional reflections also emerged in the vicinity of the central spot (circled in Fig. 2c(viii)), corresponding to interlayer ordering of $(FeO_4)_\infty$ chains in the brownmillerite structure.[38,39] After cooling to room temperature under vacuum, reflections were visible corresponding to both brownmillerite and perovskite structures, suggesting incomplete conversion of $SrFeO_{3-\delta}$ to $SrFeO_{2.5}$, and substantial heterogeneity through the depth of the sample.

The oxidation state of Fe in SFO and Ag/SFO was estimated from EELS measurements of the Fe-L_3 and Fe-L_2 energy-loss peaks performed using a TEM instrument, as described in the SI, Section S1.2, corresponding to the local Fe^{3+}/Fe^{4+} ratio. Hence, the calculated local oxygen non-stoichiometry of $SrFeO_{3-\delta}$ is shown in Fig. 3. Given that EELS measurements correspond to the loss of energy of electrons passing through the sample into the plane of the image, the estimated stoichiometry at each point corresponds to the average oxygen content through the sample along the direction of the electron beam.

From EELS measurements of unmodified SFO at room temperature, the average stoichiometry over the sample shown in Fig. 3c was estimated to be approximately $SrFeO_{2.83}$, in line with the initial stoichiometry of $SrFeO_{2.82}$ estimated from TGA measurements.[7] Given that each point in Fig. 3 corresponds to the average estimated stoichiometry through the thickness of the sample into the plane of the sample, the average of all points corresponds to the overall average for the whole three-dimensional sample; albeit with some points suggesting an unphysically high oxygen stoichiometry.

The rate of oxygen release from SFO under vacuum at room temperature was assumed to be minimal, and hence the scans at room temperature were assumed to correspond to oxygen distribution in as-prepared SFO. The distribution of oxygen within the sample was found to show some spatial variation, with a lower oxygen stoichiometry around the edge of the

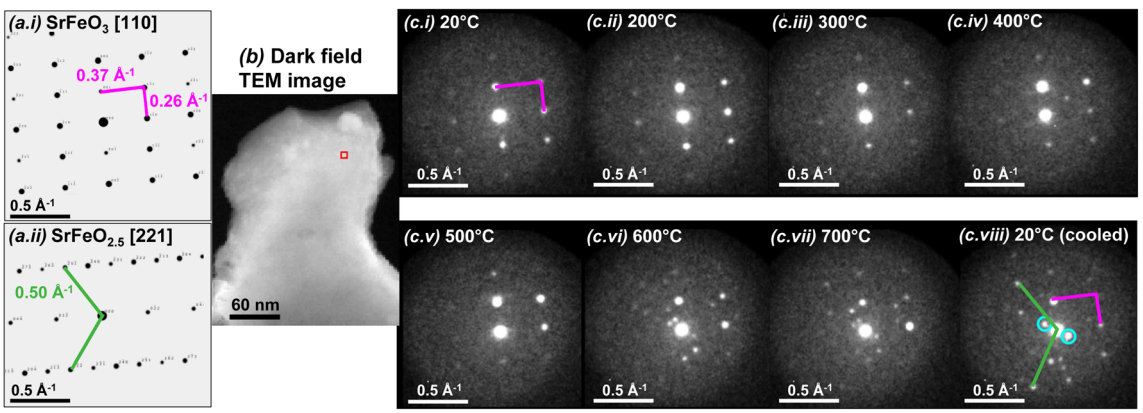

Fig. 2 (a) Simulated electron diffraction patterns along the [110] zone axis for perovskite $SrFeO_3$ with $Pm\bar{3}m$ symmetry, and along the [211] zone axis for brownmillerite $SrFeO_{2.5}$ with *Ibm*2 symmetry, (b) dark field TEM image of Ag/SFO with red square corresponding to location of SAED images, (c(i–viii)) SAED patterns of Ag/SFO collected at each temperature, with construction lines drawn to guide the eye (pink corresponding to the perovskite phase, green corresponding to the brownmillerite phase, and blue circles indicating reflections induced by $(FeO_4)_\infty$ chain ordering).

Open Access Article. Published on 26 August 2025. Downloaded on 2/23/2026 2:45:46 PM.
This article is licensed under a Creative Commons Attribution 3.0 Unported Licence.

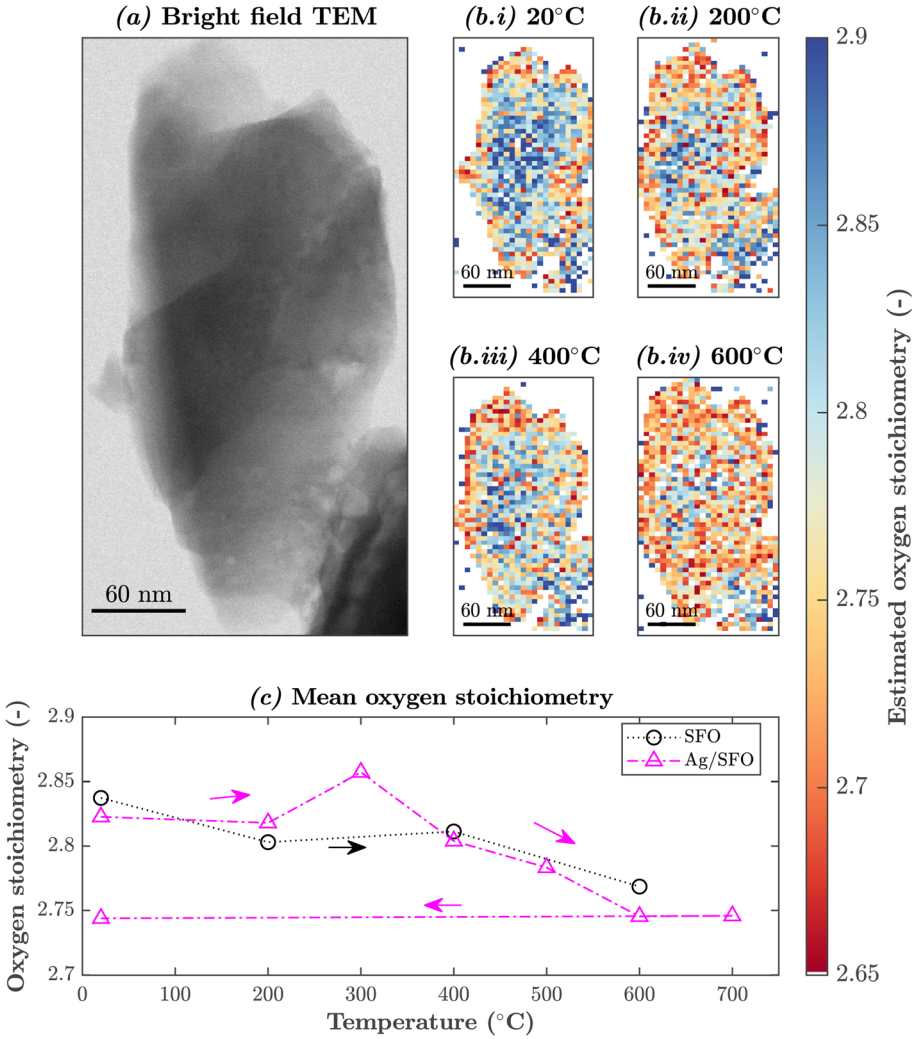

Fig. 3 *In situ* TEM images with (a) bright-field image of $SrFeO_{3-\delta}$, (b) EELS maps showing changes in local oxidation state with increasing temperature, with regions of thickness >250 nm excluded, and (c) average oxygen stoichiometry of $SrFeO_{3-\delta}$ for samples of SFO and Ag/SFO, estimated from EELS measurements under vacuum (pO_2 = *c.* 10^{-7} bar_{O_2}). Arrows in (c) indicate sequence of temperatures.

sample, and higher oxygen stoichiometry in the centre. Upon heating under vacuum, the reduced region expanded inward uniformly through the sample, with a consequent decrease in average oxygen stoichiometry, with the reduced front nearing the centre of the particle at 600 °C. The average oxygen non-stoichiometry at 600 °C was estimated to be *c.* $SrFeO_{2.77}$, higher than in isothermal TGA measurements reported previously[7] ($3 - \delta = 2.65$), where SFO was reduced in an inert atmosphere (N_2, nominal $pO_2 = 10^{-5}$ bar_{O_2}, as compared to *c.* 10^{-7} bar_{O_2} in the TEM chamber).

For Ag/SFO, a similar spatial distribution of oxygen at room temperature was observed (shown in Fig. 4), with the material showing high oxygen content near the centre of the particle, with partial reduction near the edges. The initial non-stoichiometry was estimated to be ($3 - \delta$) = 2.82, in close agreement with the TGA measurements reported in 7. From bright-field imaging and EDS measurements, two larger Ag particles (*c.* 40 nm diameter) were detected at the edge of the sample (shown in Fig. 4a and b), and a smaller Ag particle (*c.* 20 nm diameter) was found near the centre of the sample. Near the edge of the sample, small Ag nanoparticles were also visible (<10 nm, approximately equal to the spatial resolution of the EDS detector under the instrument settings used).

Upon heating Ag/SFO in the TEM, the reduced region expanded inwards from the edge of the particle, in a similar manner to SFO. Average oxygen stoichiometry declined with heating as expected as shown in Fig. 3c, with Ag/SFO showing average oxygen content equal to or lower than SFO at temperatures ≥400 °C. The apparent increase in oxygen stoichiometry between 200 °C and 300 °C was attributed to the lower quality of the scan at 300 °C (as compared to the other measurements) resulting in high uncertainty in the estimated oxygen content, rather than a genuine increase.

The reduced fronts expanded approximately uniformly through the sample, with only the thickest region at the centre of the particle remaining at higher oxygen content at 700 °C. Reduced regions of Ag/SFO were not localised around particles of Ag, suggesting that if oxygen was removed at Ag sites (as

 This journal is © The Royal Society of Chemistry 2025

Open Access Article. Published on 26 August 2025. Downloaded on 2/23/2026 2:45:46 PM. This article is licensed under a Creative Commons Attribution 3.0 Unported Licence.

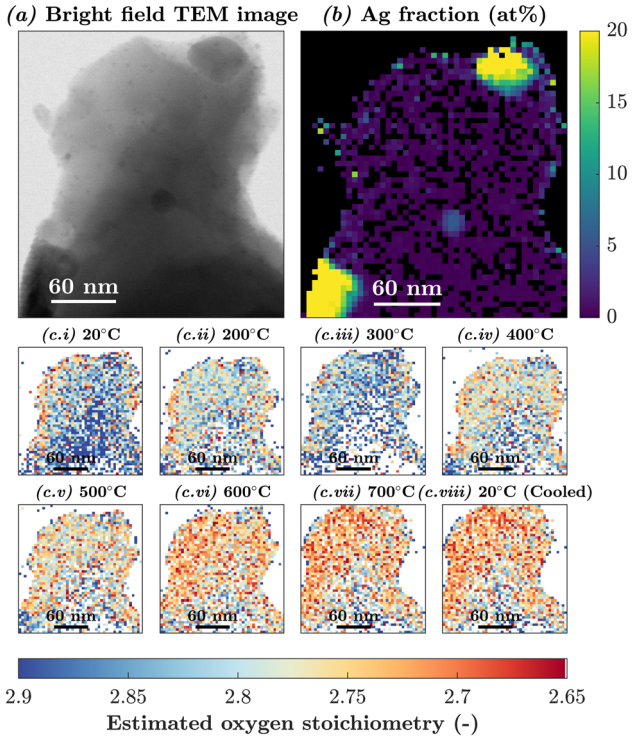

Fig. 4 *In situ* TEM images with (a) bright-field image of Ag/$SrFeO_{3-\delta}$, (b) EDS map indicating particles of Ag, (c) EELS maps showing changes in local oxidation state with increasing temperature under vacuum (pO_2 = *c.* 10^{-7} bar_{O_2}), with regions of thickness >250 nm excluded.

discussed further in Section 3.2), the transport of O^{2-} ions within the $SrFeO_3$ lattice was relatively rapid (with respect to the *c.* 10 min timescale of measurements), as any local depletion of oxygen near particles of Ag was replenished from the bulk $SrFeO_{3-\delta}$.

The final average oxygen stoichiometry at 600 °C (with little change observed upon further heating to 700 °C) was estimated at $(3-\delta) = 2.75$, less reduced than expected from TGA measurements reported in 7, where Ag/SFO stabilised at *c.* $(3-\delta) = 2.6$ after 45 min reduction in N_2 at 600 °C. Hence, either reduction of the samples was inhibited by the experimental arrangement in the TEM, or, the method of using EELS to estimate changes in oxygen non-stoichiometry tended to underestimate the extent of reduction. Upon cooling from 700 °C back to room temperature, little change in oxygen distribution was observed and average non-stoichiometry remained constant, confirming that any residual oxygen gas present in the TEM sample chamber was not sufficient to re-oxidise the Ag/SFO.

3.2 Characterisation of oxygen species

3.2.1 Near-ambient pressure X-ray photoelectron spectroscopy. To characterise the chemical environments at the surface of the samples, near-ambient pressure X-ray photoelectron spectroscopy (NAP-XPS) measurements were performed on pelletised samples of SFO and Ag/SFO. Alongside NAP-XPS measurements, photographs of the sample under investigation were taken periodically, shown in the SI, Fig. S11, with a thin orange layer of brownmillerite $SrFeO_{2.5}$ forming at the surface of each pellet under H_2, then disappearing upon exposure to O_2.

From NAP-XPS scans of the O 1s region for SFO at room temperature (shown in Fig. 5a), four distinct oxygen species were detected: $SrFeO_3$-lattice oxygen, SrO-lattice termination oxygen (*i.e.* strontium termination of the perovskite lattice in SFO[40,41]), chemisorbed oxygen species,[42–44] and residual carbonate impurities.[45,46] Residual carbonate species were detected on SFO and Ag/SFO up to 177 °C, shown in the SI, Fig. S12. For the sample of Ag/SFO at room temperature (Fig. 5d), an additional peak was detected at *c.* 532.5 eV, assigned to adsorbed Ag–O_x species.[47,48] A full description of peak fitting parameters and assignments is given in the SI, Table S3.

Upon heating SFO in 0.25 mbar H_2 (balance N_2, total pressure 5 mbar), the proportion of chemisorbed surface O species declined, with a rapid decrease above 357 °C (shown in Fig. 5b and 6a; deconvoluted XPS peaks in the SI, Fig. S14), and a corresponding increase in the relative fraction of bulk $SrFeO_3$ lattice oxygen was detected. An overall shift in binding energy for $SrFeO_3$ lattice oxygen of *c.* +1.5 eV was observed relative to the measurements at room temperature, corresponding to a shift in the chemical potential of oxygen in the reduced oxide, and hence the Fermi level.[49] The shift in Fermi level was confirmed from measurements of the Sr 3d region (shown in the SI, Fig. S13), where a similar shift (*c.* +1.5 eV) was observed, in agreement with.[49] The differences in binding energy between peaks in the O 1s spectrum remained approximately constant (±0.25 eV).

When the gas environment was switched to 1 mbar O_2, the proportion of surface oxygen species on SFO recovered rapidly, from 26.6 at% to 56.0 at% after 20 min exposure (Fig. 5c). Upon cooling back down to room temperature under 1 mbar O_2, the proportion of surface oxygen species continued to increase, reaching *c.* 65 at% at 20 °C (Fig. 6b). Additionally, two further peaks at *c.* 538–540 eV were observed, corresponding to physisorbed O_2 molecules at the surface of the sample,[50] and molecules of oxygen gas in the sample chamber.[51]

For Ag/SFO, upon heating under 0.25 mbar H_2, the proportion of surface O started to decrease at a lower temperature of 117 °C, falling to around 6 at% by 357 °C, whereupon the fraction of Ag–O_x species also began to rapidly decline (shown in Fig. 5e and 6c; deconvoluted XPS peaks in the SI, Fig. S15). The total fraction of non-lattice oxygen surface species (*i.e.* Ag–O_x plus surface O) declined steadily throughout heating under H_2, reaching 12.5 at% at 433 °C. The final fraction of surface O plus Ag–O_x on Ag/SFO was substantially lower than the fraction of surface O detected on SFO at 439 °C, showing that the presence of Ag aided the removal of surface oxygen.

When the gas environment over Ag/SFO was switched to 1 mbar O_2, the fraction of Ag–O_x species rapidly increased, reaching 37 at% within 20 min (Fig. 5f) and remaining approximately constant throughout re-oxidation (Fig. 6d). By contrast, the fraction of surface oxygen increased gradually, recovering to the initial value of 16 at% when the sample was cooled to room temperature. To better understand the

Open Access Article. Published on 26 August 2025. Downloaded on 2/23/2026 2:45:46 PM.
This article is licensed under a Creative Commons Attribution 3.0 Unported Licence.

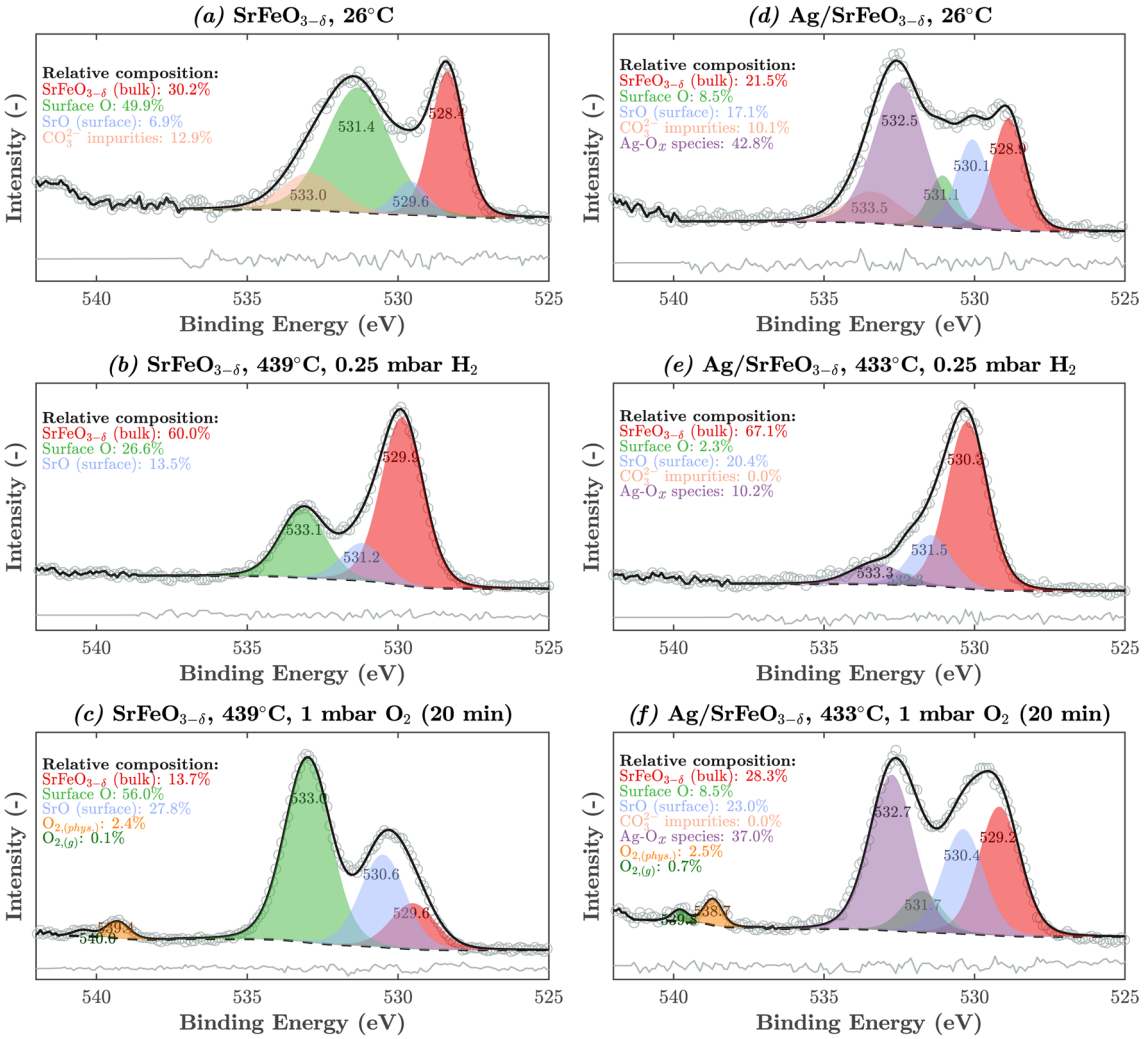

Fig. 5 NAP-XPS O 1s spectra of $SrFeO_{3-\delta}$ (a–c) and $Ag/SrFeO_{3-\delta}$ (d–f) under 0.25 mbar H_2 and 1 mbar O_2. Circles indicate experimental measurements, solid black lines indicate overall fitted curve, shaded areas correspond to individual fitted peaks, dashed lines correspond to fitted baseline, and solid grey lines correspond to difference between fitted curve and measurements. Percentage areas estimated for each peak are given, corresponding to the approximate proportion (at%) of each species at the surface.

behaviour of the surface oxygen species immediately after the gas switch from a reducing to oxidising atmosphere, rapid (20 s) scans of the O 1s region for the sample of Ag/SFO were collected, shown in Fig. 7a. Given the relatively lower resolution of the rapid scans, surface O and Ag–O_x could not be distinguished reliably, and so were fitted to a single broad peak; contributions from any other oxygen species were assumed to be negligible.

For the first 5 min after changing the set-points of the mass-flow controllers used to supply gas to the NAP-XPS sample chamber, no change was observed in the surface composition of Ag/SFO (shown in Fig. 7b), as a result of the delay between changing the gas supply, and the atmosphere around the sample changing. After approximately 5 min, the fraction of H_2 in the sample chamber began to decrease and the fraction of O_2 began to increase (monitored by online mass spectrometry, shown in Fig. 7c), and a peak at binding energy *c.* 532 eV, corresponding to the Ag–O_x and surface O species, began to emerge almost immediately, with a corresponding increase in estimated fraction of surface O and Ag–O_x species, reaching a steady state approximately 10 min after the gas switch. The position of the lattice oxygen peak also shifted back from 530 eV to *c.* 529.5 eV when the O_2 entered the sample chamber, as the surface of the sample began to re-oxidise, resulting in a partial reverse of the shift in oxygen binding energy observed previously.

3.2.2 Temperature programmed reduction (H_2-TPR). To confirm the differences in surface behaviour during reduction, H_2-TPR measurements up to 700 °C were performed for SFO and Ag/SFO, as shown in Fig. 8. During H_2-TPR, water formed as the only reaction product, with all surface carbon removed during the cleaning step in 5 vol% O_2 prior to measurements (shown in the SI, Fig. S19). During TPR measurements, the hydrogen consumption peaks corresponded to the removal of oxygen from the surface of the material, with further oxygen supplied from the bulk oxide lattice. Therefore, the presence of multiple TPR peaks represents the reaction of hydrogen with

 This journal is © The Royal Society of Chemistry 2025

Open Access Article. Published on 26 August 2025. Downloaded on 2/23/2026 2:45:46 PM.
This article is licensed under a Creative Commons Attribution 3.0 Unported Licence.

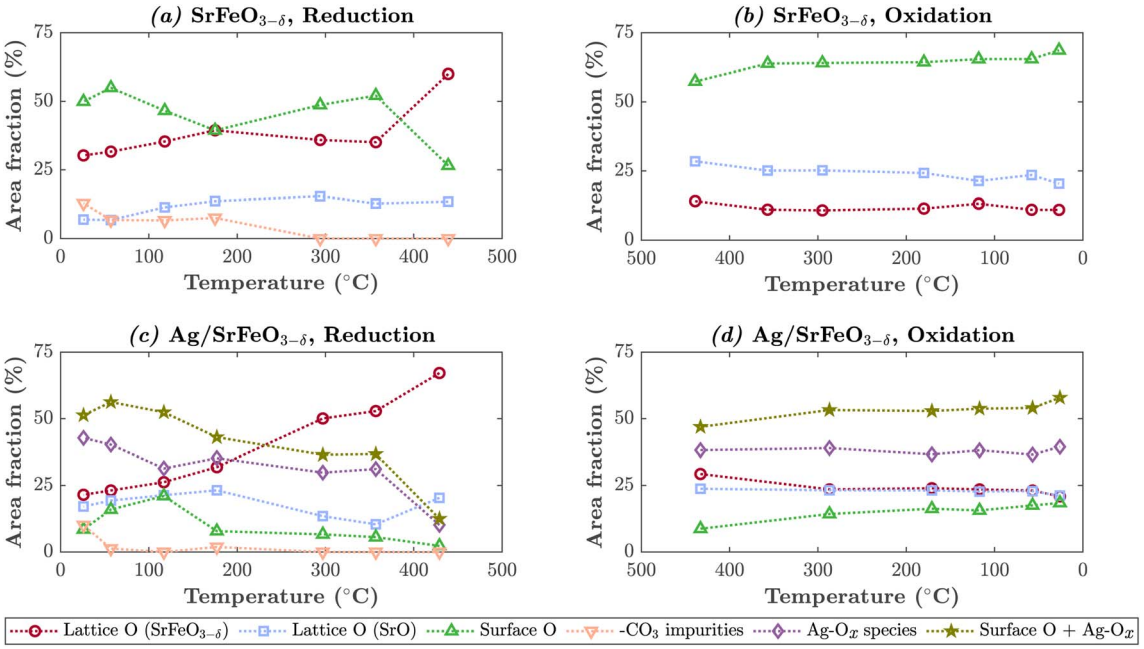

Fig. 6 Changes in surface composition with temperature for $SrFeO_{3-\delta}$ (a and b) and $Ag/SrFeO_{3-\delta}$ (c and d) under reducing (0.25 mbar H_2) and oxidising (1 mbar O_2) conditions, determined by NAP-XPS.

oxygen by differing mechanisms and with distinct surface species.[13,52]

The sample of SFO showed a single peak in hydrogen consumption, centred at around 412 °C. Contrastingly, the sample of Ag/SFO showed two distinct features: a large, broad peak centred at around 216 °C, and a shallower peak centred at around 428 °C. The differences between the two samples under H_2-TPR suggest that the peak at 216 °C for Ag/SFO corresponded to reaction of H_2 with adsorbed $Ag–O_x$ surface species, as detected by NAP-XPS, discussed in further detail in Section

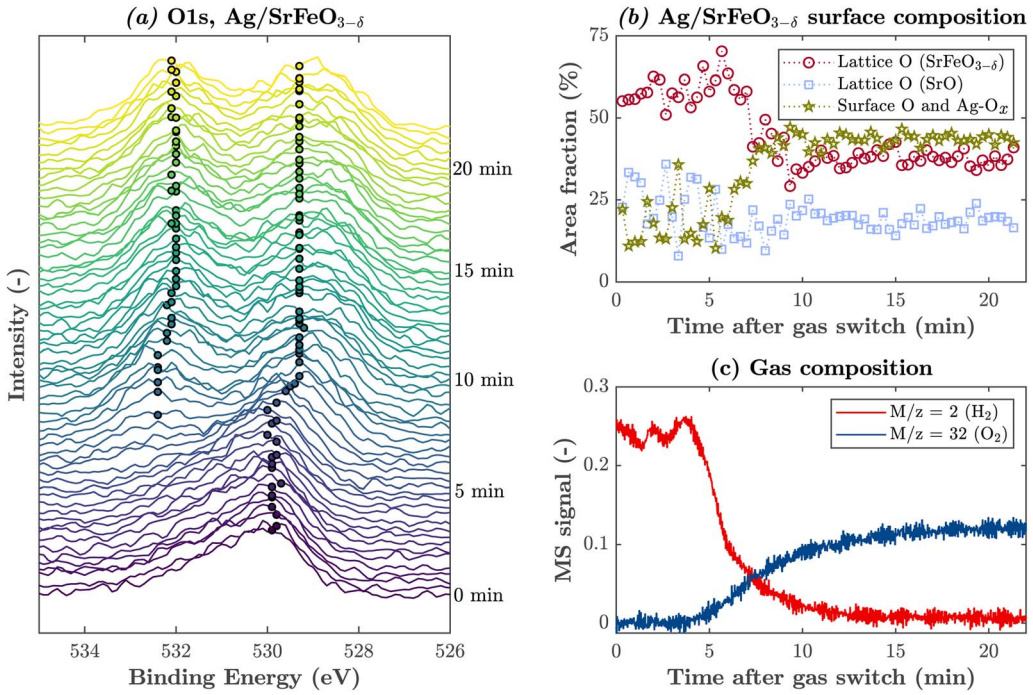

Fig. 7 (a) Rapid (20 s) scans of O 1s region immediately after gas switch from 0.25 mbar H_2 to 1 mbar O_2 at 433 °C (line colour indicates time after gas switch to differentiate successive scans, where purple = immediately after gas switch, yellow = after 20 min of exposure to O_2). Markers indicate fitted peak centre positions for lattice O in $SrFeO_{3-\delta}$, and surface O and $Ag–O_x$. (b) Estimated composition of surface species after gas switch. (c) Composition of gas in sample chamber, measured by online mass spectrometry.

Open Access Article. Published on 26 August 2025. Downloaded on 2/23/2026 2:45:46 PM.
This article is licensed under a Creative Commons Attribution 3.0 Unported Licence.

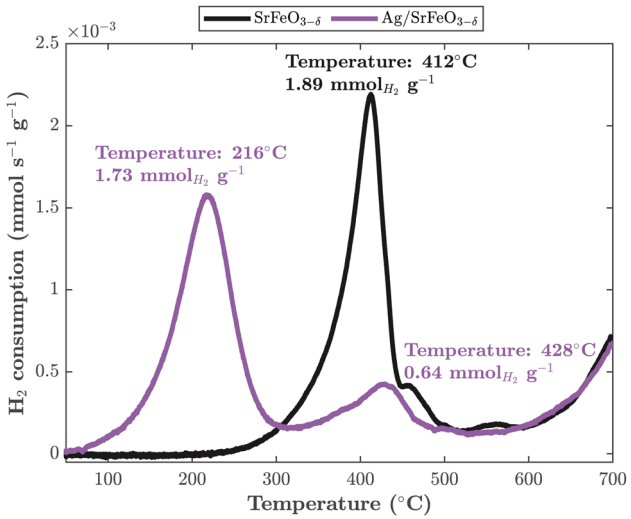

Fig. 8 Temperature-programmed reduction of SFO and Ag/SFO in 5 vol% H_2, with temperatures corresponding to centre of each fitted component, and total H_2 consumption for each feature. Samples were cleaned *in situ* of carbonate and other impurities at 650 °C in 5 vol% O_2 for 2 h prior collecting the TPR measurements shown in the figure.

4.2.1, and that the peaks at 412–428 °C corresponded to the reduction of bulk SFO. Total cumulative hydrogen consumption at 700 °C was lower for SFO than Ag/SFO, at around 1.9 and 2.4 $mmol_{H_2}\ g^{-1}$, respectively, corresponding to an estimated final non-stoichiometry of approximately $(3-\delta) = 2.5$ for SFO, as expected for reduction in H_2 up to 700 °C from XRD measurements, to form brownmillerite $SrFeO_{2.5}$. The estimated final stoichiometry of Ag/SFO was somewhat lower, at $(3-\delta) = 2.4$, suggesting possible further deep reduction of the $SrFeO_{2.5}$ to form *e.g.* Ruddlesden-Popper phases,[5] or, slightly lower initial oxygen stoichiometry for the sample of Ag/SFO,[7] resulting in an underestimate of the final oxygen content.

3.2.3 ***In situ*** **Raman spectroscopy.** Raman spectroscopy with simultaneous heating under 5 vol% H_2 was used to identify the Ag–O_x species detected at the surface of Ag/SFO from NAP-XPS and H_2-TPR, with the measured spectra shown in Fig. 9a. All samples were calcined overnight in air prior to collecting Raman spectra, to remove surface impurities. The shaded bands span reported wavenumber ranges of peaks corresponding to different Ag–O_x species: atomic Ag–O (*i.e.* chemisorbed oxygen atoms) at 680–800 cm^{-1}, peroxide Ag–O_2^{2-} at 880–1020 cm^{-1}, and superoxide Ag–O_2^{-} at 1020–1080 cm^{-1} (ref. 53–56) (with values from literature summarised in the SI, Table

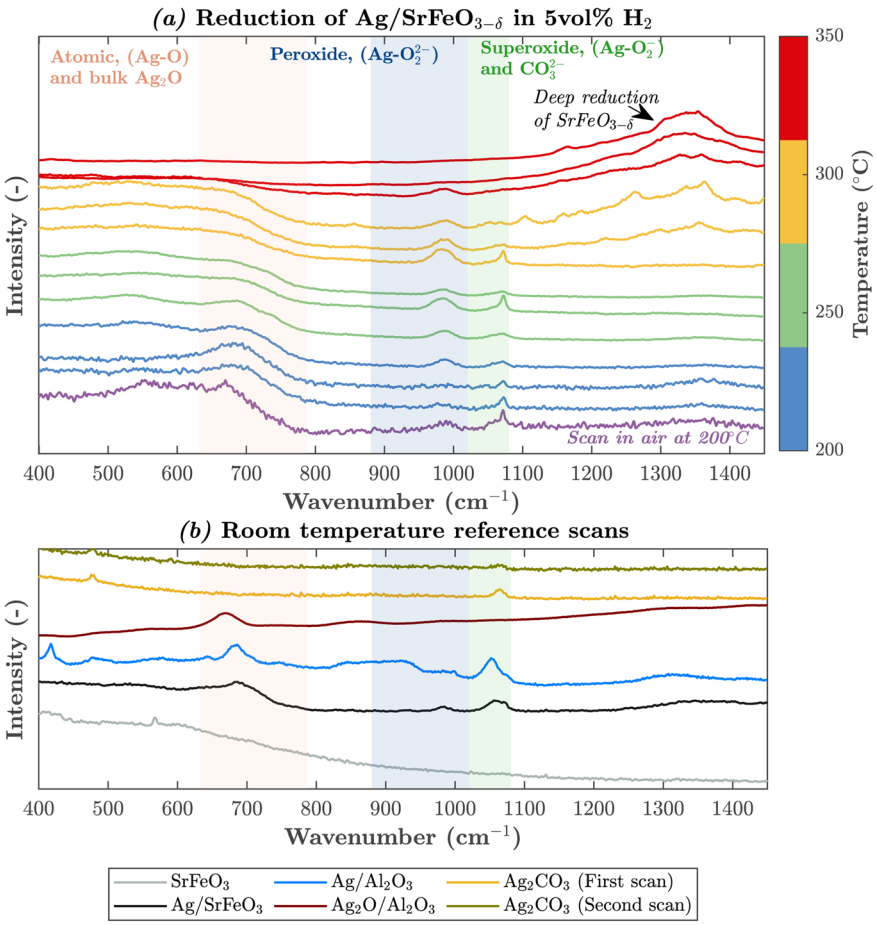

Fig. 9 (a) *In situ* Raman spectroscopy of Ag/$SrFeO_{3-\delta}$ showing removal of O_x surface species under 5 vol% H_2, with shaded wavenumber ranges from literature, (b) reference scans at room temperature. Reference scans are normalised with respect to maximum intensity detected in each scan.

 This journal is © The Royal Society of Chemistry 2025

Open Access Article. Published on 26 August 2025. Downloaded on 2/23/2026 2:45:46 PM. This article is licensed under a Creative Commons Attribution 3.0 Unported Licence.

S4), with some overlap between Ag–O and silver oxide (bulk Ag_2O), and between Ag–O_2^{2-} and Ag_2CO_3, shown in Fig. 9b.

For Ag/SFO at room temperature in air, clear peaks were observed in the wavenumber ranges corresponding to atomic Ag–O (at *c.* 670 cm^{-1}), peroxide Ag–O_2^- (at *c.* 989 cm^{-1}), and superoxide Ag–O^{2-} (at *c.* 1072 cm^{-1}). No peaks in the regions of interest were observed on bare SFO without Ag, indicating minimal contribution from carbonate impurities or other species in the SFO support, as $SrCO_3$ has a characteristic Raman band at around 1071 cm^{-1}.[57] For Ag on Al_2O_3, strong Raman bands were detected at 686 and 1052 cm^{-1}, assigned to atomic oxygen and superoxide, respectively. A very weak band was detected at 990 cm^{-1}, suggesting that some peroxide Ag–O_2^{2-} was present on the Ag/Al_2O_3.[56] The sample of Ag_2O/Al_2O_3 showed a Raman peak at around 668 cm^{-1}, at slightly lower wavenumber than the peak detected in the Ag–O region for Ag/Al_2O_3 and Ag/SFO. The sample of Ag_2CO_3 showed a peak at 1065 cm^{-1}, overlapping with the superoxide region, which halved in intensity upon collecting a second scan at the same point, as a result of damage to the photosensitive sample from the laser beam.[58]

Upon heating the sample of Ag/SFO to 200 °C in air (purple curve), all three main peaks at 670, 989, and 1072 cm^{-1} remained, although the relative intensity of the atomic oxygen and superoxide peaks somewhat declined, possibly indicating removal of trace silver oxide and carbonate contaminants. With gas flow through the sample stage switched to 5 vol% H_2 in N_2 (blue curves), little change was observed at 200 °C, then, upon heating to 250 °C (green curves), the intensity of the peak corresponding to atomic oxygen declined, and almost entirely disappeared after three scans (*c.* 15 min dwell time at 250 °C). With further heating to 300 °C (yellow curves), the atomic oxygen feature at 670 cm^{-1} fully disappeared, and over the course of three successive scans, the intensity of the peak at 1072 cm^{-1} (assigned to superoxide) began to decline. At the highest temperature point of 350 °C (red curves), the superoxide peak disappeared entirely, and after two scans, the peroxide peak at 989 cm^{-1} also disappeared. In addition, a prominent feature at *c.* 1350 cm^{-1} emerged, attributable to two-magnon scattering in brownmillerite $SrFeO_{2.5}$.[59,60] Deep reduction of $SrFeO_{3-\delta}$ ($3-\delta \leq 2.5$) and possible formation of brownmillerite $SrFeO_{2.5}$ at the surface of the sample pellet was in line with Fig. S11, where an orange brownmillerite surface layer formed at the surface of the $SrFeO_{3-\delta}$ pellet under reducing conditions at *c.* 350 °C.

4 Discussion

4.1 Bulk reduction of $SrFeO_{3-\delta}$

The XRD results in Fig. 1 show that for reduction in 5 vol% H_2, the presence of Ag on $SrFeO_{3-\delta}$ aided phase transition from perovskite to brownmillerite, decreasing the temperature required by 200 °C as compared to unmodified SFO.

Wang *et al.*[8] showed from high-temperature XRD measurements that noble metals deposited on strontium perovskites reduced the temperature required for transformation from perovskite to brownmillerite by about 150 °C, investigated using thin-film samples. From density functional theory calculations and TEM imaging of the Ag–$SrFeO_{3-\delta}$, the authors postulated that the presence of the noble metal film aided oxygen release by donating electrons to the perovskite support, weakening Fe–O bonds by forming an amorphous interfacial layer of Ag–O–Fe. However, given the authors focused on thin films, they did not consider the effects from interfacial reactions of Ag, which will be more relevant in the polycrystalline samples considered here, as discussed in Section 4.2.1.

The TEM images, with parallel EDS and EELS mapping, shown in Fig. 3 and 4 demonstrate the changes in Fe oxidation state, and hence oxygen stoichiometry in $SrFeO_{3-\delta}$, during heating *in vacuo* for SFO and Ag/SFO.

The sample of Ag/SFO did not show significant localisation of reduced areas at or near particles of Ag – instead, both samples showed growth of reduced fronts moving inwards to the centre of the particle in an approximately uniform manner. The lack of spatial variation near particles of Ag in Ag/SFO was in contrast with *in situ* TEM studies of other noble metal–metal oxide systems under redox reactions. For particles of Pd on $CeO_{2-\delta}$,[61] a reduced region of Ce^{3+} at the Pd–$CeO_{2-\delta}$ interface spread through the bulk Ce^{4+} during reduction. In contrast, *in situ* EELS and NAP-XPS studies of $NiFe_2O_4$ nanoparticles without any metal catalysts under strong reducing conditions (H_2 or CO at ≥850 °C) showed little variation in Fe valence for the first 120 min,[62,63] requiring deep overall reduction of the oxide for concentration gradients to develop.

Hence, for the experimental conditions applied here in the TEM, with Ag/SFO uncoupling oxygen into vacuum, given the Ag/SFO system did not show localisation of reduced regions around Ag, relatively rapid transport of O^{2-} ions within the $SrFeO_{3-\delta}$ lattice might have been sufficient to dissipate any spatial gradients in oxygen content near Ag resulting from oxygen removal at Ag–$SrFeO_{3-\delta}$ interfaces. Instead, the particle became reduced gradually from the edge to the centre, with transport of oxygen from the core to the surface, resulting in a front of lower-valence Fe^{3+} moving inwards from the edge of the particle to the centre.

Additionally, electron diffraction images shown in Fig. 2 suggested partial formation of a brownmillerite phase in Ag/SFO at elevated temperature (≥600 °C). However, the diffraction patterns also showed the clear presence of reflections corresponding to a cubic perovskite phase alongside the brownmillerite, indicating heterogeneity through the sample depth, possibly with thin layers of brownmillerite forming at external surfaces around a perovskite core. The relatively slow phase transition in TEM experiments is in contrast with the rapid phase transition observed in studies of $SrFeO_{3-\delta}$ thin films,[64] where brownmillerite regions expanded through the sample, surrounding 'islands' of unconverted perovskite.

At 700 °C, the average oxygen stoichiometry at the point on the sample where a brownmillerite phase was visible (shown in Fig. 2b) was estimated to be *c.* $SrFeO_{2.67}$, exceeding $(3-\delta) = 2.5$ as would be expected for pure brownmillerite, and hence further suggesting a mixture of perovskite and brownmillerite through the sample depth. Alternatively, the higher than expected stoichiometry might indicate formation of hyper-

Open Access Article. Published on 26 August 2025. Downloaded on 2/23/2026 2:45:46 PM. This article is licensed under a Creative Commons Attribution 3.0 Unported Licence.

stoichiometric material with brownmillerite structure ($SrFeO_{2.5+\delta}$).[64]

4.2 Surface reactions and mechanisms of oxygen transport

4.2.1 Changes in surface species during reduction. From NAP-XPS measurements, shown in Fig. 5 and 6, multiple different oxygen species were detected at the surface of SFO and Ag/SFO, with the relative fraction of each species varying substantially with temperature. For both SFO and Ag/SFO, upon heating from room temperature to ≥430 °C in hydrogen, the proportion of oxygen surface species decreased, with a rapid decline in chemisorbed oxygen on SFO above 357 °C.

The decrease in surface oxygen for SFO under heating is in good agreement with the findings of Crumlin *et al.*,[42] where thin film and pelletised samples of $La_{0.8}Sr_{0.2}CoO_{3-\delta}$ perovskite were heated under 1 mbar O_2 up to 520 °C. At 220 °C, peaks in the O 1s spectrum were detected corresponding to chemisorbed surface oxygen species, lattice oxygen in the bulk perovskite, and oxygen in a surface termination layer of SrO,[40,41] as in Fig. 5. For the pelletised sample, the proportion of surface oxygen decreased by around 11% upon heating to 520 °C, whereas, for the thin film sample, surface oxygen decreased by around 7% upon heating to 370 °C, and disappeared entirely at 520 °C (with only lattice oxygen in the bulk $La_{0.8}Sr_{0.2}CoO_{3-\delta}$ and the surface termination layer of SrO remaining).

Here, using 0.25 mbar H_2 to reduce $SrFeO_{3-\delta}$ based materials, surface oxygen content decreased by around 46 at% upon heating from room temperature to 439 °C. However, the persistence of surface oxygen even at high temperatures under a relatively strong reducing gas indicated the difficulty of removing surface oxygen from SFO in the absence of Ag, especially for bulk samples rather than thin films where surface oxygen can be replenished by diffusion within particles of SFO.

The samples of Ag/SFO investigated here showed markedly different behaviour during reduction as compared to unmodified SFO, with the emergence of an additional O 1s peak at high binding energy corresponding to Ag–O_x surface species. In studies of oxygen adsorbed on foil and powder samples of pure Ag, Rocha *et al.*[65] assigned peaks in the O 1s region to a series of surface and sub-surface Ag–O species – here, however, the overlap between peaks corresponding to oxygen in Ag–O_x, lattice $SrFeO_3$, and the SrO surface termination layer meant that Ag–O_x were grouped into a single, relatively broad peak (with FWHM constrained to ≤ 2 eV). Additionally, under the conditions investigated here, the fraction of low binding energy (≤528 eV) Ag–O species on Ag/SFO was negligible, as expected for measurements taken at or above room temperature.[66]

During reduction in H_2, the decrease in the relative area fraction of the Ag–O_x peak with successive measurements suggested removal of oxygen by reaction with hydrogen at the surface of Ag. At each temperature investigated, the fraction of Ag–O_x greatly exceeded the fraction of chemisorbed oxygen at the surface of $SrFeO_{3-\delta}$, and the chemisorbed oxygen on $SrFeO_{3-\delta}$ was removed at lower temperatures for the sample of Ag/SFO than for bare SFO. During heating, the fraction of oxygen at the surface of $SrFeO_{3-\delta}$ decreased at lower temperatures than Ag–O_x, reaching <10 at% at 177 °C, whereas Ag–O_x species gradually decreased up to 357 °C, then decreased sharply to *c.* 10 at% at 433 °C.

Hence, the greater fraction of Ag–O_x species than adsorbed oxygen on SFO might indicate that at elevated temperatures, lattice oxygen from the $SrFeO_{3-\delta}$ support was transported from the bulk to the surface, then rapidly migrated to Ag sites, with little chemisorbed oxygen remaining at the surface of the SFO. Given the final fraction of total surface oxygen was approximately 50% lower for Ag/SFO than SFO at >430 °C, the mechanism of reduction probably proceeded *via* Ag facilitating removal of oxygen by forming reactive Ag–O_x intermediate species, which were then able to react with hydrogen more easily than oxygen on bare SFO, possibly by altering the mechanism of reaction between the H_2 and oxygen.[16]

For SFO, the relative fraction of bulk $SrFeO_{3-\delta}$ lattice oxygen sharply decreased upon exposure to oxygen gas, and the area fraction of the peak corresponding to oxygen in SrO increased, with the relative fractions of all species remaining approximately constant through further cooling. The increase in the area of the peak corresponding to SrO could indicate a consolidation of the SrO lattice termination layer during re-oxidation after the sample had been deeply reduced. Consolidation of the SrO surface layer would be consistent with the increase in the ratio of peak areas between the Sr 3d and Fe 2p binding energy regions (shown in the SI, Fig. S16) during re-oxidation.

During rapid scans of the O 1s region during re-oxidation of Ag/SFO at 439 °C, shown in Fig. 7, the peak corresponding to surface oxygen species emerged almost instantaneously as concentration of O_2 in the sample chamber rose. The centre of the lattice oxygen peak began to shift to lower binding energy by 0.5 eV over 20 min, partially reversing the positive shift during heating associated with a change in the chemical potential of lattice oxygen for reduced samples.[49] Upon further cooling of Ag/SFO, the fraction of Ag–O_x species remained approximately constant, and the fraction of surface O species increased; Ag–O_x remained the dominant surface oxygen species at all temperatures during re-oxidation. Moreover, the ratio of chemisorbed oxygen on SFO to the sum of total oxygen excluding Ag–O_x species (*i.e.* the oxygen on the surface of $SrFeO_{3-\delta}$, or in the $SrFeO_{3-\delta}$ lattice only, shown in the SI, Fig. S17), the total concentration of adsorbed O on Ag/SFO was lower than for SFO at all temperatures, but rose more rapidly with sequential cooling during re-oxidation.

Hence, the NAP-XPS measurements during re-oxidation suggest that the mechanism of oxidation for Ag/SFO might proceed by oxygen initially being adsorbed from the gas phase to form surface Ag–O_x species, followed by relatively rapid incorporation of oxygen into the $SrFeO_{3-\delta}$ lattice as the bulk SFO support re-oxidised. A similar mechanism has been suggested for ionic membranes for oxygen separation promoted with Ag,[10,67] where Ag particles catalyse oxygen dissociation on the feed side, to allow monoatomic $O_{lattice}$ species to pass through the membrane to the permeate. Here, the Ag might act as a 'gateway' for oxygen dissociation and incorporation into Ag/SFO during re-oxidation, in a manner analogous to the

 This journal is © The Royal Society of Chemistry 2025

Open Access Article. Published on 26 August 2025. Downloaded on 2/23/2026 2:45:46 PM. This article is licensed under a Creative Commons Attribution 3.0 Unported Licence.

behaviour observed for CeO_2 in grafted CeO_2–Fe_2O_3 composites,[68] and in mixed Ag–CeO_2–$SrFeO_{3-\delta}$ materials.[2]

Furthermore, during reduction and oxidation under NAP-XPS, sulphur impurities on the surface of Ag, reported to act as promotors for olefin epoxidation over Ag,[66,69,70] were found to undergo redox activity, discussed in the SI, Section S4. During reduction in H_2, sulphate (Ag_2SO_x) impurities were reduced to sulphide (Ag_2S), with the sulphate species restored during exposure to O_2 (shown in the SI, Fig. S18)

The findings from H_2-TPR of Ag/SFO aligned with studies of Ag supported on $CeO_{2-\delta}$,[16] where the presence of Ag aided removal of oxygen from CeO_2, resulting in a shift in the peak corresponding to reduction of bulk $CeO_{2-\delta}$ from 529 °C to 494 °C, and introduced a new peak at 100–300 °C corresponding to removal of surface oxygen from silver.

Assuming that the only consumption of hydrogen during H_2-TPR was reaction with oxygen to form water (as shown from the MS traces during H_2-TPR in the SI, Fig. S19), the number of moles of H_2 consumed should equal the number of moles of O atoms removed from the samples. Hence, the total H_2 consumption in the lower temperature feature for Ag/SFO exceeded the theoretical amount of oxygen available from adsorbed oxygen on Ag by three orders of magnitude, estimated at 6.4 $\mu mol_{O,ads}\ g^{-1}$ for 10 wt% Ag on $SrFeO_{3-\delta}$ assuming full surface coverage of adsorbed oxygen,[31] and was three times larger than the maximum oxygen available if all Ag was present as Ag_2O, estimated at 0.46 mmol g^{-1}.[31] Therefore, for the sample of Ag/SFO, the additional oxygen removal at lower temperature came at the expense of oxygen removal in the peaks at *c.* 500 °C.

Moreover, the consumption of hydrogen at low temperatures (<300 °C, well below the ignition temperature of H_2 in O_2)[71] over Ag/SFO was in agreement with previous studies of catalytic combustion of H_2 over Ag. Dokuchits *et al.* demonstrated that during combustion of H_2 in O_2 in the presence of particles of metallic Ag, O_2 molecules adsorbed on the surface of Ag and dissociated to form reactive surface Ag–O species,[72,73] which then reacted with H_2 to form H_2O in the temperature range 150–200 °C.[74]

Hence, the H_2-TPR results support the hypothesis established here that for Ag/SFO, oxygen is removed from the bulk of $SrFeO_{3-\delta}$ during reduction *via* the formation of Ag–O_x intermediates, allowing reaction at lower temperatures than for bare $SrFeO_{3-\delta}$. The relatively broad peak in H_2 consumption over the range 150–300 °C observed for Ag/SFO was assigned to the removal of Ag–O, Ag–O_2^-, and Ag–O_2^{2-} surface species as identified from Raman spectroscopy in Fig. 9.

4.2.2 Proposed mechanisms of oxygen transport. Initial studies of the Ag/$SrFeO_{3-\delta}$ system[1,2,75] hypothesised that oxygen migrated from the $SrFeO_{3-\delta}$ lattice to the surface of Ag by diffusion of monoatomic oxygen species through bulk Ag, to form atomic Ag–O surface species which were then removed during reaction with a reducing gas (shown in Fig. 10a). However, other mechanisms of oxygen transport are possible for oxygen release in metal–metal oxide systems, including spillover of oxygen from the surface of the oxide to the adsorb at the surface of the metal[9,76] (shown in Fig. 10b), and *vice-versa* during absorption of oxygen from the gas phase into the oxide support.[10]

When oxygen is removed from the lattice of $SrFeO_{3-\delta}$ during reduction, the initial state is as monoatomic $O_{lattice}^{2-}$ ions, and hence the presence of diatomic peroxide and superoxide species at the surface of Ag/SFO detected by Raman spectroscopy (shown in Fig. 9) was somewhat surprising. To explain the presence of Ag–O_2^- and Ag–O_2^{2-} at the surface of Ag/SFO, the diatomic oxygen species might act as an intermediate during the formation of atomic Ag–O species.

Deng *et al.*[77] found that during methanol oxidation in air with *in situ* Raman spectrocopy, Ag–O_2^{2-} (peroxide) species were formed by absorption of O_2 from the gas phase, and then dissociated to form reactive Ag–O species. Additionally, previous studies of chemical looping over iron-based oxygen carriers[63,78,79] suggested that oxygen species at the surface of the oxide reach a dynamic equilibrium of the form $2O_{lattice}^{2-} \rightleftharpoons 2O_{ads}^{2-} \rightleftharpoons 2O_{ads}^{-} \rightleftharpoons O_{2,ads}^{2-} \rightleftharpoons O_{2,ads}^{-} \rightleftharpoons O_{2,gas}$, with interconversion between lattice oxygen ions and diatomic species. Huang *et al.*[79] proposed that during reduction of $NiFe_2O_4$ in H_2, the mechanism of reduction proceeded by $O_{lattice}^{2-}$ ions combining at the surface of the oxide to form peroxide O_2^{2-}, which then reacted with H_2 by forming hydroxyl OH^- ions, and ultimately water. Gao *et al.*[80] also determined that during chemical looping dehydrogenation of ethane over Li_2CO_3/

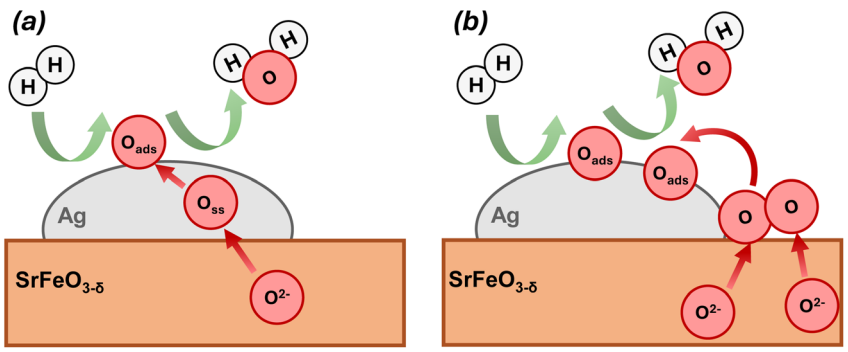

Fig. 10 Simplified mechanisms proposed for oxygen transport from bulk $SrFeO_{3-\delta}$ to the surface of Ag nanoparticles: (a) diffusion through bulk Ag, proposed by Chan *et al.*,[1] (b) spillover of oxygen at the Ag–$SrFeO_{3-\delta}$-gas interface, analogous to the mechanism of oxygen removal from Ag/$CeO_{2-\delta}$ proposed by Lee *et al.*[9]

Open Access Article. Published on 26 August 2025. Downloaded on 2/23/2026 2:45:46 PM. This article is licensed under a Creative Commons Attribution 3.0 Unported Licence.

$La_xSr_{1-x}FeO_{3-\delta}$ composites, peroxide species formed at the Li_2CO_3-$La_xSr_{1-x}FeO_{3-\delta}$ interface by reduction of Fe^{4+} to Fe^{3+}, then acted as the active species in the oxidation reaction.

Hence, if similar reactions of $O_{lattice}^{2-}$ ions to form peroxide ions occurred in $SrFeO_{3-\delta}$, the mechanism of reduction could proceed by spillover of the peroxide ion at the Ag–$SrFeO_{3-\delta}$ interface to form Ag–O_2^{2-} on Ag, followed by dissociation to form Ag–O species, which react with the reducing gas (as shown in Fig. 10b). A summary of the proposed mechanism is given in Fig. 11, showing the catalytic reduction pathway *via* reaction between H_2 and Ag–O_x species at relatively low temperatures, and direct reaction between H_2 and $SrFeO_{3-\delta}$ at higher temperatures.

Furthermore, when a sample of Ag/$SrFeO_{3-\delta}$ pre-reduced under 5 vol% H_2 in the Raman stage for 20 min at 250 °C was exposed to air (shown in the SI, Fig. S21), the intensity of the Raman peak corresponding to peroxide species rapidly increased, suggesting that reoxidation of the material proceeded *via* initial formation of diatomic surface Ag–O_2^{2-} species, followed by incorporation of atomic oxygen into the $SrFeO_{3-\delta}$ lattice.

However, the potential role of the superoxide Ag–O_2^- species in such a mechanism remains unclear.

In the absence of spillover of diatomic species at the Ag–$SrFeO_{3-\delta}$ interface (*i.e.* if oxygen transport proceeded primarily *via* diffusion of monoatomic species through Ag, as shown in Fig. 10a), a different explanation for the presence of diatomic oxygen species would be required. Given the material was exposed to air prior to reduction, diatomic species might have formed at the surface of Ag from adsorption of molecular oxygen.[81] Therefore, if atomic Ag–O species were preferentially removed by H_2 (as indicated by the rapid decline in atomic oxygen Raman peak intensity with heating), the residual diatomic species might act as relatively inert spectator molecules. Then, upon heating to higher temperature, the diatomic species could react with hydrogen and become removed, but otherwise have little role in the transport of oxygen from $SrFeO_{3-\delta}$. However, from the H_2-TPR measurements of Ag/SFO reported in Fig. 8, the peak assigned to surface oxygen species comprised 1.73 mmol g^{-1} of oxygen removed, greatly exceeding the maximum estimated amount of adsorbed O_2 on Ag (6.4 μmol g^{-1}).[31] Hence, adsorbed oxygen gas from air could account for at most 0.4 at% of total surface oxygen detected (with the remaining 99.6 at% assigned to atomic oxygen species). However, the peaks in the Raman spectra shown in Fig. 9 for Ag/SFO corresponding to atomic and diatomic oxygen species were similar in intensity, rendering such a large difference in the relative proportions of each species unlikely.

Additionally, from cyclic measurements of Ag_2O/Al_2O_3 under a reducing atmosphere (5 vol% H_2) at 200 °C (shown in the SI, Fig. S20), the feature at 668 cm^{-1} assigned to Ag_2O oxide declined, indicating reduction to metallic silver. Upon switching to an oxidising atmosphere (compressed air), the intensity of the Ag_2O feature continued to decline, and fully disappeared after switching back to a reducing atmosphere. Little change in the Raman spectrum was observed in subsequent gas switching cycles at higher temperatures, suggesting that bulk Ag_2O was not present in substantial quantities at the surface of Ag/$SrFeO_{3-\delta}$ during redox cycling.

Therefore, the diatomic oxygen species detected on Ag probably formed as an intermediate in the overall mechanism of reduction, rather than being merely residual chemisorbed oxygen from air, suggesting that diffusion of monoatomic oxygen through Ag is not the only process involved in the removal of oxygen from Ag/SFO materials.

The reaction mechanisms proposed here assume that adsorption of hydrogen species on Ag was negligible relative to oxygen, as determined from mechanistic studies of hydrogen combustion with gaseous oxygen over Ag.[73,82] Here, $H_{2(g)}$ was used as a model reducing agent to react with the chemisorbed oxygen species and leave as $H_2O_{(g)}$, as described in previous studies of hydrogen combustion over Ag.[73]

However, in more complicated chemical looping processes where hydrocarbons react selectively with adsorbed oxygen species on catalysts containing Ag to form oxygenated products,

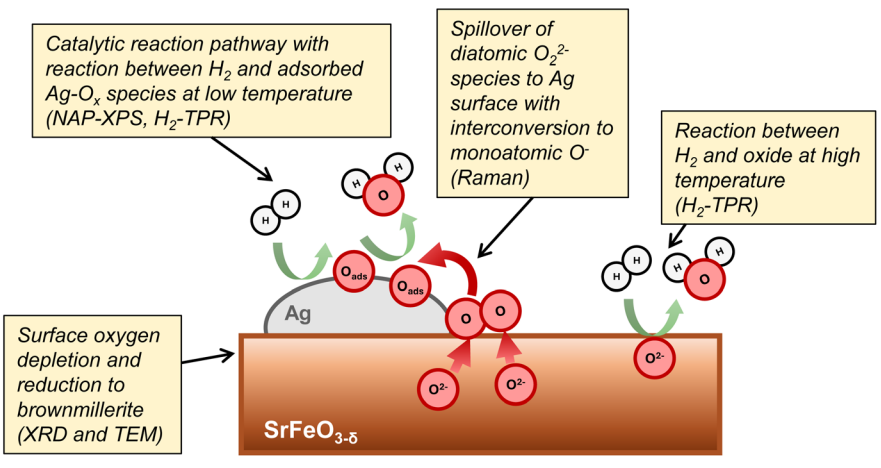

Fig. 11 Proposed reaction mechanisms during reduction of Ag/$SrFeO_{3-\delta}$, with formation of diatomic and monoatomic Ag–O_x species. The techniques used in this work to identify each element of the reaction are indicated in parentheses.

 This journal is © The Royal Society of Chemistry 2025

Open Access Article. Published on 26 August 2025. Downloaded on 2/23/2026 2:45:46 PM. This article is licensed under a Creative Commons Attribution 3.0 Unported Licence.

hydrogen has been postulated to participate in surface reactions,[83] although the full mechanisms remain uncertain.

The relative distribution of Ag–O_x species on nanoparticles of Ag was found by Li *et al.*[56] to be affected by interactions between the Ag and the support (in their study, α-Al_2O_3 or SiO_2). When the materials were used as catalysts for the epoxidation of olefins (*e.g.* ethylene) by O_2, Ag–O_2^- species favoured the epoxide product, and Ag–O and Ag–O_2^{2-} species favoured the complete combustion pathway. Lee *et al.*[13] also found that when using Ag/$CeO_{2-\delta}$ as a catalyst for the oxidation of soot, the proportion of different oxygen species was influenced by the concentration of oxygen vacancies in the vicinity of the Ag, with higher concentrations of vacancies favouring Ag–O and Ag–O_2^- over Ag–O_2^{2-}. During chemical looping processes, the number of oxygen vacancies in the oxygen carrier support changes continuously during each reduction cycle as the material donates oxygen to the reaction, meaning the distribution of selective and non-selective surface species might vary over the course of each reduction step. Furthermore, in a microkinetic study of ethylene epoxidation over Ag catalysts, Setiawan *et al.*[84] determined that the most likely pathway for reaction proceeded by adsorption of $O_{2,(g)}$ to form subsurface diatomic Ag–O_2 species, with interconversion to monoatomic Ag–O. From density functional theory calculations (DFT), the authors predicted that for reactions over Ag(111) surfaces, both Ag–O_2 and Ag–O could react with C_2H_4 to form oxygenated products *via* multiple surface reaction pathways; hence, an analogous network of reaction mechanisms might proceed for epoxidation in a chemical looping mode, with formation of monoatomic Ag–O and diatomic Ag–O_2 species from lattice oxygen.

Furthermore, previous studies investigating chemical looping selective oxidation determined that surface modification of La_x-$Sr_{1-x}FeO_{3-\delta}$ with Li_2CO_3 promoters favoured the formation and transport of peroxide species.[80] Hence, to further understand the mechanisms of reactions of oxygen in Ag/$SrFeO_{3-\delta}$ materials during chemical looping, future work should consider whether the trends in desorption of surface species under H_2 apply in other environments (*e.g.* olefins), and, whether modification of the $SrFeO_{3-\delta}$ support (*e.g.* doping with other elements) influences the mechanism of reduction and distribution of oxygen surface species. This study also confirmed that the addition of an Ag catalyst increased the chemical potential of oxygen in the SFO oxygen carrier, allowing the material to be adjusted to promote reactions requiring a specific oxygen carrier potential, such as oxidative dehydrogenation of hydrocarbons[85,86] and alcohols.[4,87]

Additionally, by applying isotopic exchange, with a sample of Ag/$SrFeO_{3-\delta}$ exposed successively to $^{18}O_2$ and either H_2 or *e.g.* an olefin, the selective and non-selective oxygen species on Ag/$SrFeO_{3-\delta}$ (*i.e.* atomic, peroxide, and superoxide oxygen) could be distinguished using parallel Raman spectroscopy and mass spectrometry.[88,89] New materials could then be developed with surface modification to favour selective oxygen species, and to inhibit non-selective reaction pathways.

5 Conclusions

In this work, the presence of Ag nanoparticles at the surface of particles of $SrFeO_{3-\delta}$ was found to strongly influence the reactive properties during reduction in H_2. From *in situ* XRD experiments, the sample of Ag/$SrFeO_{3-\delta}$ underwent phase transition to brownmillerite $SrFeO_{2.5}$ under 5 vol% H_2 at 300 °C, as compared to unmodified $SrFeO_{3-\delta}$ which remained in the perovskite phase up to 500 °C. Both materials rapidly returned to perovskite form after switching to air at 800 °C. From TEM experiments, heating $SrFeO_{3-\delta}$ and Ag/$SrFeO_{3-\delta}$ from room temperature to 700 °C, both samples showed a decrease in average oxygen stoichiometry, with reduced regions moving inwards from the edge of the particles. However, for Ag/$SrFeO_{3-\delta}$, localised reduction in the vicinity of nanoparticles of Ag was not observed, suggesting that transport of oxygen within the solid material was relatively rapid as compared to the rate of removal at the surface.

From NAP-XPS measurements during reduction and oxidation, chemisorbed oxygen on $SrFeO_{3-\delta}$ was observed to deplete during a temperature ramp in hydrogen, with the sample of Ag/$SrFeO_{3-\delta}$ showing a more rapid rate of depletion, and, the presence of Ag–O_x surface species. At the highest temperatures investigated (433–439 °C), the total content of adsorbed oxygen species on Ag/$SrFeO_{3-\delta}$ was around 47% lower than for $SrFeO_{3-\delta}$, suggesting that reactive Ag–O_x species aided the removal of oxygen by the H_2 reducing agent. The Ag–O_x surface species were assigned from Raman spectroscopy to atomic Ag–O, peroxide Ag–O_2^{2-}, and superoxide Ag–O_2^-. A potential mechanism for reduction was proposed by which Ag could act as an oxygen 'gateway', where lattice oxygen from $SrFeO_{3-\delta}$ was transported to the surface of Ag by spillover at the Ag–$SrFeO_{3-\delta}$ interface to form Ag–O_2^{2-} species, which then dissociated to form atomic Ag–O. Our results provide new mechanistic insights into the bulk and surface behaviour of oxygen carriers during redox cycling, allowing for development of novel materials with accelerated oxygen transport for low temperature applications of chemical looping.

Conflicts of interest

The authors declare that they have no known competing financial interests or personal relationships that could have appeared to influence the work reported in this paper.

Data availability

Additional data used to support the findings of this study are available in the SI. Primary data and analysis code can be provided by the corresponding authors upon reasonable request.

Supplementary information is available: collection and processing of TEM measurements, additional XRD measurements, additional NAP-XPS spectra and fitting parameters, redox activity of sulphur impurities from NAP-XPS, additional H_2-TPR measurements, and additional Raman spectroscopy measurements. See DOI: **https://doi.org/10.1039/d5ta04944j**.

Acknowledgements

ARPH acknowledges funding from EPSRC studentship grant no. 2376181, the Cambridge School of Technology Vice-

Open Access Article. Published on 26 August 2025. Downloaded on 2/23/2026 2:45:46 PM. This article is licensed under a Creative Commons Attribution 3.0 Unported Licence.

Chancellor's Award, and travel grants from the Royal Society of Chemistry and the Cambridge Philosophical Society. JMAS acknowledges support from the EPSRC Cambridge NanoCDT, EP/L015978/1. This project was supported in part by the Henry Royce Institute Researcher Equipment Access Schemes, EPSRC Grant Numbers EP/P022464/1 and EP/R00661X/1. We acknowledge use of the Thermo Fisher Spectra 300 TEM funded by EPSRC under grant EP/R008779/1. We acknowledge support from the Henry Royce Institute (EPSRC grants: EP/P022464/1, EP/R00661X/1), which funded the VXSF Facilities (https://engineering.leeds.ac.uk/vxsf) within the Bragg Centre for Materials Research at Leeds. Many thanks are given to Amy Xu for assistance in generating simulated electron diffraction patterns, and to Alexander Oing for advice regarding Raman spectroscopy measurements.

References

1 M. S. C. Chan, E. Marek, S. A. Scott and J. S. Dennis, Chemical looping epoxidation, *J. Catal.*, 2018, **359**, 1–7, DOI: 10.1016/j.jcat.2017.12.030.

2 E. J. Marek, S. Gabra, J. S. Dennis and S. A. Scott, High selectivity epoxidation of ethylene in chemical looping setup, *Appl. Catal., B*, 2020, **262**, 118216, DOI: 10.1016/j.apcatb.2019.118216.

3 S. Gabra, E. J. Marek, S. Poulston, G. Williams and J. S. Dennis, The use of strontium ferrite perovskite as an oxygen carrier in the chemical looping epoxidation of ethylene, *Appl. Catal., B*, 2021, **286**, 119821, DOI: 10.1016/j.apcatb.2020.119821.

4 J. C. Gebers, A. F. B. Abu Kasim, G. J. Fulham, K. Y. Kwong and E. J. Marek, Production of Acetaldehyde *via* Oxidative Dehydrogenation of Ethanol in a Chemical Looping Setup, *ACS Eng. Au*, 2023, **3**(3), 184–194, DOI: 10.1021/acsengineeringau.2c00052.

5 E. Marek, W. Hu, M. Gaultois, C. P. Grey and S. A. Scott, The use of strontium ferrite in chemical looping systems, *Appl. Energy*, 2018, **223**, 369–382, DOI: 10.1016/j.apenergy.2018.04.090.

6 W. Chang, Y. Hu, W. Xu, C. Huang, H. Chen, J. He, Y. Han, Y. Zhu, X. Ma and X. Wang, Recent Advances of Oxygen Carriers for Hydrogen Production *via* Chemical Looping Water-Splitting, *Catalysts*, 2023, **13**(2), 279, DOI: 10.3390/CATAL13020279.

7 A. R. P. Harrison, K. Y. Kwong, Y. Zheng, A. Balkrishna, A. Dyson and E. J. Marek, Kinetic and Thermodynamic Enhancement of Low-Temperature Oxygen Release from Strontium Ferrite Perovskites Modified with Ag and CeO 2, *Energy Fuels*, 2023, **37**(13), 9487–9499, DOI: 10.1021/acs.energyfuels.3c01263.

8 Q. Wang, Y. Gu, W. Zhu, L. Han, F. Pan and C. Song, Noble-Metal-Assisted Fast Interfacial Oxygen Migration with Topotactic Phase Transition in Perovskite Oxides, *Adv. Funct. Mater.*, 2021, **31**(50), 2106765, DOI: 10.1002/adfm.202106765.

9 J. H. Lee, D. Y. Jo, J. W. Choung, C. H. Kim, H. C. Ham and K.-Y. Lee, Roles of noble metals (M = Ag, Au, Pd, Pt and Rh) on CeO2 in enhancing activity toward soot oxidation: Active oxygen species and DFT calculations, *J. Hazard. Mater.*, 2021, **403**, 124085, DOI: 10.1016/j.jhazmat.2020.124085.

10 A. Leo, S. Liu and J. C. Diniz da Costa, The enhancement of oxygen flux on Ba0.5Sr0.5Co0.8Fe0.2O3δ (BSCF) hollow fibers using silver surface modification, *J. Membr. Sci.*, 2009, **340**(1–2), 148–153, DOI: 10.1016/j.memsci.2009.05.022.

11 I. V. Kovalev, I. A. Mal'bakhova, A. M. Vorob'ev, T. A. Borisenko, M. P. Popov, A. A. Matvienko, A. I. Titkov and A. P. Nemudryi, Microtube Membranes for the Selective Synthesis of Oxygen and Hydrogen, *Russ. J. Electrochem.*, 2021, **57**(10), 1019–1027, DOI: 10.1134/S1023193521100074.

12 A. J. Majewski and A. Dhir, Application of silver in microtubular solid oxide fuel cells, *Mater. Renew. Sustain. Energy*, 2018, **7**(3), 1–13, DOI: 10.1007/S40243-018-0123-Y.

13 J. H. Lee, S. H. Lee, J. W. Choung, C. H. Kim and K.-Y. Lee, Ag-incorporated macroporous CeO2 catalysts for soot oxidation: Effects of Ag amount on the generation of active oxygen species, *Appl. Catal., B*, 2019, **246**, 356–366, DOI: 10.1016/j.apcatb.2019.01.064.

14 H. Wang, S. Liu, Z. Zhao, X. Zou, M. Liu, W. Liu, X. Wu and D. Weng, Activation and deactivation of Ag/CeO2 during soot oxidation: influences of interfacial ceria reduction, *Catal. Sci. Technol.*, 2017, **7**(10), 2129–2139, DOI: 10.1039/C7CY00450H.

15 M. V. Grabchenko, G. V. Mamontov, V. I. Zaikovskii, V. La Parola, L. F. Liotta and O. V. Vodyankina, Design of Ag-CeO2/SiO2 catalyst for oxidative dehydrogenation of ethanol: Control of Ag–CeO2 interfacial interaction, *Catal. Today*, 2019, **333**, 2–9, DOI: 10.1016/j.cattod.2018.05.014.

16 J. Wang, X. Lai, H. Zhang, X. Zhou, T. Lin, J. Wang and Y. Chen, Low-temperature toluene oxidation on Ag/CexZr1-xO2 monolithic catalysts: Synergistic catalysis of silver and ceria-zirconia, *Combust. Flame*, 2023, **248**, 112577, DOI: 10.1016/j.combustflame.2022.112577.

17 R. Merkle and J. Maier, How Is Oxygen Incorporated into Oxides? A Comprehensive Kinetic Study of a Simple Solid-State Reaction with SrTiO3 as a Model Material, *Angew. Chem., Int. Ed.*, 2008, **47**(21), 3874–3894, DOI: 10.1002/ANIE.200700987.

18 A. A. Coelho, TOPAS and TOPAS-Academic: an optimization program integrating computer algebra and crystallographic objects written in C++, *J. Appl. Crystallogr.*, 2018, **51**(1), 210–218, DOI: 10.1107/S1600576718000183.

19 A. Belsky, M. Hellenbrandt, V. L. Karen and P. Luksch, New developments in the Inorganic Crystal Structure Database (ICSD): accessibility in support of materials research and design, *Acta Crystallogr., Sect. B:Struct. Sci.*, 2002, **58**(3), 364–369, DOI: 10.1107/s0108768102006948.

20 F. d. l. Pena, T. Ostasevicius, V. T. Fauske, P. Burdet, P. Jokubauskas, M. Nord, M. Sarahan, E. Prestat, D. N. Johnstone, J. Taillon, J. Caron, T. Furnival, K. E. MacArthur, A. Eljarrat, S. Mazzucco, V. Migunov, T. Aarholt, M. Walls, F. Winkler, G. Donval, B. Martineau, A. Garmannslund, L.-F. Zagonel and I. Iyengar, Electron

 This journal is © The Royal Society of Chemistry 2025

Open Access Article. Published on 26 August 2025. Downloaded on 2/23/2026 2:45:46 PM. This article is licensed under a Creative Commons Attribution 3.0 Unported Licence.

Microscopy (Big and Small) Data Analysis With the Open Source Software Package HyperSpy, *Microsc. Microanal.*, 2017, **23**(S1), 214–215, DOI: **10.1017/S1431927617001751**.

21 P. A. Van Aken and B. Liebscher, Quantification of ferrous/ferric ratios in minerals: New evaluation schemes of Fe L23 electron energy-loss near-edge spectra, *Phys. Chem. Miner.*, 2002, **29**(3), 188–200, DOI: **10.1007/S00269-001-0222-6**.

22 H. Tan, J. Verbeeck, A. Abakumov and G. Van Tendeloo, Oxidation state and chemical shift investigation in transition metal oxides by EELS, *Ultramicroscopy*, 2012, **116**, 24–33, DOI: **10.1016/j.ultramic.2012.03.002**.

23 R. Lopez-Adams, S. M. Fairclough, I. C. Lyon, S. J. Haigh, J. Zhang, F. J. Zhao, K. L. Moore and J. R. Lloyd, Elucidating heterogeneous iron biomineralization patterns in a denitrifying As(iii)-oxidizing bacterium: implications for arsenic immobilization, *Environ. Sci.: Nano*, 2022, **9**(3), 1076–1090, DOI: **10.1039/D1EN00905B**.

24 P. M. Dietrich, D. R. Baer, F. Mirabella and A. Thissen, Description and operation characteristics of SPECS EnviroESCA, *Surf. Sci. Spectra*, 2025, **32**(1), 013001, DOI: **10.1116/6.0003878**.

25 L. Pielsticker, R. Nicholls, S. Beeg, C. Hartwig, G. Klihm, R. Schlögl, S. Tougaard and M. Greiner, Inelastic electron scattering by the gas phase in near ambient pressure XPS measurements, *Surf. Interface Anal.*, 2021, **53**(7), 605–617, DOI: **10.1002/sia.6947**.

26 N. Fairley, V. Fernandez, M. Richard-Plouet, C. Guillot-Deudon, J. Walton, E. Smith, D. Flahaut, M. Greiner, M. Biesinger, S. Tougaard, D. Morgan and J. Baltrusaitis, Systematic and collaborative approach to problem solving using X-ray photoelectron spectroscopy, *Appl. Surf. Sci. Adv.*, 2021, **5**, 100112, DOI: **10.1016/j.apsadv.2021.100112**.

27 D. A. Shirley, High-Resolution X-Ray Photoemission Spectrum of the Valence Bands of Gold, *Phys. Rev. B*, 1972, **5**(12), 4709, DOI: **10.1103/PhysRevB.5.4709**.

28 M. C. Biesinger, Accessing the robustness of adventitious carbon for charge referencing (correction) purposes in XPS analysis: Insights from a multi-user facility data review, *Appl. Surf. Sci.*, 2022, **597**, 153681, DOI: **10.1016/J.APSUSC.2022.153681**.

29 P. Norby, R. Dinnebier and A. N. Fitch, Decomposition of silver carbonate; the crystal structure of two high-temperature modifications of Ag2Co3, *Inorg. Chem.*, 2002, **41**(14), 3628–3637, DOI: **10.1021/ic0111177**.

30 G. I. N. Waterhouse, G. A. Bowmaker and J. B. Metson, The thermal decomposition of silver (I, III) oxide: A combined XRD, FT-IR and Raman spectroscopic study, *Phys. Chem. Chem. Phys.*, 2001, **3**(17), 3838–3845, DOI: **10.1039/b103226g**.

31 J. C. Gebers, A. R. P. Harrison and E. J. Marek, How does the oxidation and reduction time affect the chemical looping epoxidation of ethylene?, *Discover Chem. Eng.*, 2022, **2**(1), 4, DOI: **10.1007/s43938-022-00011-4**.

32 O. A. Savinskaya, A. P. Nemudry, A. N. Nadeev and S. V. Tsybulya, Synthesis and study of the thermal stability of SrFe1 xM xO3 z (M = Mo, W) perovskites, *Solid State Ionics*, 2008, **179**(21–26), 1076–1079, DOI: **10.1016/J.SSI.2008.02.005**.

33 I. Starkov, S. Bychkov, A. Matvienko and A. Nemudry, Oxygen release technique as a method for the determination of "δ–pO 2 –T" diagrams for MIEC oxides, *Phys. Chem. Chem. Phys.*, 2014, **16**(12), 5527–5535, DOI: **10.1039/C3CP52143E**.

34 W. Hu, F. Donat, S. A. Scott and J. S. Dennis, Kinetics of oxygen uncoupling of a copper based oxygen carrier, *Appl. Energy*, 2016, **161**, 92–100, DOI: **10.1016/J.APENERGY.2015.10.006**.

35 D. D. Taylor, N. J. Schreiber, B. D. Levitas, W. Xu, P. S. Whitfield and E. E. Rodriguez, Oxygen Storage Properties of La 1– x Sr x FeO 3δ for Chemical-Looping Reactions—An *In Situ* Neutron and Synchrotron X-ray Study, *Chem. Mater.*, 2016, **28**(11), 3951–3960, DOI: **10.1021/acs.chemmater.6b01274**.

36 J. P. Hodges, S. Short, J. D. Jorgensen, X. Xiong, B. Dabrowski, S. M. Mini and C. W. Kimball, Evolution of Oxygen-Vacancy Ordered Crystal Structures in the Perovskite Series SrnFenO3n1 (n=2, 4, 8, and), and the Relationship to Electronic and Magnetic Properties, *J. Solid State Chem.*, 2000, **151**(2), 190–209, DOI: **10.1006/JSSC.1999.8640**.

37 M. Schmidt and S. J. Campbell, Crystal and Magnetic Structures of Sr2Fe2O5 at Elevated Temperature, *J. Solid State Chem.*, 2001, **156**(2), 292–304, DOI: **10.1006/JSSC.2000.8998**.

38 M. Batuk, D. Vandemeulebroucke, M. Ceretti, W. Paulus and J. Hadermann, Topotactic redox cycling in SrFeO2.5+δ explored by 3D electron diffraction in different gas atmospheres, *J. Mater. Chem. A*, 2023, **11**(1), 213–220, DOI: **10.1039/D2TA03247C**.

39 H. D'Hondt, A. M. Abakumov, J. Hadermann, A. S. Kalyuzhnaya, M. G. Rozova, E. V. Antipov and G. Van Tendeloo, Tetrahedral Chain Order in the Sr 2 Fe 2 O 5 Brownmillerite, *Chem. Mater.*, 2008, **20**(22), 7188–7194, DOI: **10.1021/cm801723b**.

40 G. M. Rupp, A. K. Opitz, A. Nenning, A. Limbeck and J. Fleig, Real-time impedance monitoring of oxygen reduction during surface modification of thin film cathodes, *Nat. Mater.*, 2017, **16**(6), 640–645, DOI: **10.1038/nmat4879**.

41 A. Zhu, D. Li, T. Zhu and X. Zhu, Tailored SrFeO3-δ for chemical looping dry reforming of methane, *Green Chem. Eng.*, 2024, **6**(1), 102–115, DOI: **10.1016/J.GCE.2024.04.003**.

42 E. J. Crumlin, E. Mutoro, Z. Liu, M. E. Grass, M. D. Biegalski, Y. L. Lee, D. Morgan, H. M. Christen, H. Bluhm and Y. Shao-Horn, Surface strontium enrichment on highly active perovskites for oxygen electrocatalysis in solid oxide fuel cells, *Energy Environ. Sci.*, 2012, **5**(3), 6081–6088, DOI: **10.1039/C2EE03397F**.

43 K. A. Stoerzinger, L. Wang, H. Su, K.-J. Lee, E. J. Crumlin and Y. Du, Influence of strain on SrFeO3-δ oxidation, reduction, and water dissociation: Insights from ambient pressure X-ray photoelectron spectroscopy, *Appl. Surf. Sci.*, 2020, **527**, 146919, DOI: **10.1016/j.apsusc.2020.146919**.

44 Y. Zhou, Z. Zhou, J. Sun, L. Liu, F. Luo, G. Xu, X. E. Cao and M. Xu, Ruddlesden-Popper-type perovskite Sr3Fe2O7δ for

Open Access Article. Published on 26 August 2025. Downloaded on 2/23/2026 2:45:46 PM. This article is licensed under a Creative Commons Attribution 3.0 Unported Licence.

enhanced thermochemical energy storage, *EcoMat*, 2023, **5**(7), 12347, DOI: 10.1002/EOM2.12347.

45 H. Falcón, J. A. Barbero, J. A. Alonso, M. J. Martínez-Lope and J. L. G. G. Fierro, SrFeO 3 - δ Perovskite Oxides: Chemical Features and Performance for Methane Combustion, *Chem. Mater.*, 2002, **14**(5), 2325–2333, DOI: 10.1021/cm011292l.

46 A. Abd El-Naser, E. K. Abdel-Khalek, E. Nabhan, D. A. Rayan, M. S. Gaafar and N. S. Abd El-Aal, Study the influence of oxygen-deficient ($\delta = 0.135$) in SrFeO 3-δ nanoparticles perovskite on structural, electrical and magnetic properties, *Philos. Mag.*, 2021, **101**(6), 710–728, DOI: 10.1080/14786435.2020.1862427.

47 G. Schön, ESCA Studies of Ag, Ag2O and AgO, *Acta Chem. Scand.*, 1973, **27**, 2623–2633, DOI: 10.3891/acta.chem.scand.27-2623.

48 T. Pu, A. Setiawan, B. Mosevitzky Lis, M. Zhu, M. E. Ford, S. Rangarajan and I. E. Wachs, Nature and Reactivity of Oxygen Species on/in Silver Catalysts during Ethylene Oxidation, *ACS Catal.*, 2022, **12**(8), 4375–4381, DOI: 10.1021/acscatal.1c05939.

49 A. Nenning, A. K. Opitz, C. Rameshan, R. Rameshan, R. Blume, M. Hävecker, A. Knop-Gericke, G. Rupprechter, B. Klötzer and J. Fleig, Ambient pressure XPS study of mixed conducting perovskite-type SOFC cathode and anode materials under well-defined electrochemical polarization, *J. Phys. Chem. C*, 2016, **120**(3), 1461–1471, DOI: 10.1021/ACS.JPCC.5B08596/.

50 C. Puglia, A. Nilsson, B. Hernnäs, O. Karis, P. Bennich and N. Mårtensson, Physisorbed, chemisorbed and dissociated O2 on Pt(111) studied by different core level spectroscopy methods, *Surf. Sci.*, 1995, **342**(1–3), 119–133, DOI: 10.1016/0039-6028(95)00798-9.

51 T. G. Avval, S. Chatterjee, G. T. Hodges, S. Bahr, P. Dietrich, M. Meyer, A. Thißen and M. R. Linford, Oxygen gas, O2(g), by near-ambient pressure XPS, *Surf. Sci. Spectra*, 2019, **26**(1), 014021, DOI: 10.1116/1.5100962.

52 D. Chen, D. He, J. Lu, L. Zhong, F. Liu, J. Liu, J. Yu, G. Wan, S. He and Y. Luo, Investigation of the role of surface lattice oxygen and bulk lattice oxygen migration of cerium-based oxygen carriers: XPS and designed H2-TPR characterization, *Appl. Catal., B*, 2017, **218**, 249–259, DOI: 10.1016/j.apcatb.2017.06.053.

53 C. B. Wang, G. Deo and I. E. Wachs, Interaction of Polycrystalline Silver with Oxygen, Water, Carbon Dioxide, Ethylene, and Methanol: *In Situ* Raman and Catalytic Studies, *J. Phys. Chem. B*, 1999, **103**(27), 5645–5656, DOI: 10.1021/JP984363L.

54 Z. Zhao and M. A. Carpenter, Support-Free Bimodal Distribution of Plasmonically Active Ag/AgO x Nanoparticle Catalysts: Attributes and Plasmon Enhanced Surface Chemistry, *J. Phys. Chem. C*, 2013, **117**(21), 11124–11132, DOI: 10.1021/jp400837r.

55 H. A. Alzahrani and J. J. Bravo-Suárez, *In situ* Raman spectroscopy study of silver particle size effects on unpromoted Ag/α-Al2O3 during ethylene epoxidation with molecular oxygen, *J. Catal.*, 2023, **418**, 225–236, DOI: 10.1016/J.JCAT.2023.01.016.

56 R. Li, C. Liu, Y. Fan, Q. Fu and X. Bao, Metal-oxide interaction modulating activity of active oxygen species on atomically dispersed silver catalyst, *Chem. Commun.*, 2023, **59**, 3854–3857, DOI: 10.1039/D3CC00617D.

57 W. Kaabar, S. Bott and R. Devonshire, Raman spectroscopic study of mixed carbonate materials, *Spectrochim. Acta, Part A*, 2011, **78**(1), 136–141, DOI: 10.1016/J.SAA.2010.09.011.

58 G. Dai, J. Yu and G. Liu, A New Approach for Photocorrosion Inhibition of Ag 2 CO 3 Photocatalyst with Highly Visible-Light-Responsive Reactivity, *J. Phys. Chem. C*, 2012, **116**(29), 15519–15524, DOI: 10.1021/jp305669f.

59 O. I. Barkalov, S. V. Zaitsev and V. D. Sedykh, Strontium ferrite SrFeO3-δ (2.50 3-δ 2.87) studied by Raman and Mössbauer spectroscopy, *Solid State Commun.*, 2022, **354**, 114912, DOI: 10.1016/j.ssc.2022.114912.

60 A. S. Anokhin, A. G. Razumnaya, V. I. Torgashev, V. G. Trotsenko, Y. I. Yuzyuk, A. A. Bush, V. Y. Shkuratov, B. P. Gorshunov, E. S. Zhukova, L. S. Kadyrov and G. A. Komandin, Dynamic spectral response of solid solutions of the bismuth-strontium ferrite Bi1 x Sr x FeO3 δ in the frequency range 0.3–200 THz, *Phys. Solid State*, 2013, **55**(7), 1417–1430, DOI: 10.1134/S1063783413070032.

61 A. H. Mahadi, L. Ye, S. M. Fairclough, J. Qu, S. Wu, W. Chen, E. I. Papaioannou, B. Ray, T. J. Pennycook, S. J. Haigh, N. P. Young, K. Tedsree, I. S. Metcalfe and S. C. E. Tsang, Beyond surface redox and oxygen mobility at pd-polar ceria (100) interface: Underlying principle for strong metal-support interactions in green catalysis, *Appl. Catal., B*, 2020, **270**, 118843, DOI: 10.1016/j.apcatb.2020.118843.

62 D. Song, Y. Lin, S. Fang, Y. Li, K. Zhao, X. Chen, Z. Huang, F. He, Z. Zhao, H. Huang and F. Li, Unraveling the atomic interdiffusion mechanism of NiFe2O4 oxygen carriers during chemical looping CO2 conversion, *Carbon Energy*, 2024, **6**(8), e493, DOI: 10.1002/CEY2.493.

63 D. Song, Y. Lin, K. Zhao, Z. Huang, F. He and Y. Xiong, Migration Mechanism of Lattice Oxygen: Conversion of CO2 to CO Using NiFe2O4 Spinel Oxygen Carrier in Chemical Looping Reactions, *Catalysts*, 2022, **12**(10), 1181, DOI: 10.3390/catal12101181.

64 Y. Xing, I. Kim, K. T. Kang, B. Park, Z. Wang, J. Chan Kim, H. Y. Jeong, W. S. Choi, J. Lee and S. H. Oh, Atomic-scale operando observation of oxygen diffusion during topotactic phase transition of a perovskite oxide, *Matter*, 2022, **5**(9), 3009–3022, DOI: 10.1016/j.matt.2022.06.013.

65 T. C. R. R. Rocha, A. Oestereich, D. V. Demidov, M. Hävecker, S. Zafeiratos, G. Weinberg, V. I. Bukhtiyarov, A. Knop-Gericke and R. Schlögl, The silver–oxygen system in catalysis: new insights by near ambient pressure X-ray photoelectron spectroscopy, *Phys. Chem. Chem. Phys.*, 2012, **14**(13), 4554, DOI: 10.1039/c2cp22472k.

66 E. A. Carbonio, T. C. R. Rocha, A. Y. Klyushin, I. Píš, E. Magnano, S. Nappini, S. Piccinin, A. Knop-Gericke, R. Schlögl and T. E. Jones, Are multiple oxygen species selective in ethylene epoxidation on silver?, *Chem. Sci.*, 2018, **9**(4), 990–998, DOI: 10.1039/C7SC04728B.

 This journal is © The Royal Society of Chemistry 2025

Open Access Article. Published on 26 August 2025. Downloaded on 2/23/2026 2:45:46 PM. This article is licensed under a Creative Commons Attribution 3.0 Unported Licence.

67 C. Yacou, A. Leo, J. Motuzas, S. Smart, S. Zhang, S. Liu and J. C. Diniz da Costa, High oxygen production membranes by Ag catalytic surface modified BSCC perovskite, *Sep. Purif. Technol.*, 2023, **317**, 123829, DOI: 10.1016/j.seppur.2023.123829.

68 M. Machida, T. Kawada, H. Fujii and S. Hinokuma, The Role of CeO2 as a Gateway for Oxygen Storage over CeO2-Grafted Fe2O3 Composite Materials, *J. Phys. Chem. C*, 2015, **119**(44), 24932–24941, DOI: 10.1021/ACS.JPCC.5B09876.

69 T. E. Jones, R. Wyrwich, S. Böcklein, E. A. Carbonio, M. T. Greiner, A. Y. Klyushin, W. Moritz, A. Locatelli, T. O. Menteş, M. A. Niño, A. Knop-Gericke, R. Schlögl, S. Günther, J. Wintterlin and S. Piccinin, The Selective Species in Ethylene Epoxidation on Silver, *ACS Catal.*, 2018, **8**(5), 3844–3852, DOI: 10.1021/acscatal.8b00660.

70 E. A. Carbonio, F. Sulzmann, A. Y. Klyushin, M. Hävecker, S. Piccinin, A. Knop-Gericke, R. Schlögl and T. E. Jones, Adjusting the Chemical Reactivity of Oxygen for Propylene Epoxidation on Silver by Rational Design: The Use of an Oxyanion and Cl, *ACS Catal.*, 2023, **13**(9), 5906–5913, DOI: 10.1021/acscatal.3c00297.

71 K. G. Falk, The ignition temperatures of hydrogen-oxygen mixtures, *J. Am. Chem. Soc.*, 1906, **28**(11), 1517–1534, DOI: 10.1021/JA01977A001.

72 E. V. Dokuchits, A. V. Khasin and A. A. Khassin, Interaction of hydrogen and water with oxygen adsorbed on silver, *React. Kinet., Mech. Catal.*, 2011, **103**(2), 261–266, DOI: 10.1007/S11144-011-0319-Y.

73 E. V. Dokuchits, A. V. Khasin and A. A. Khassin, Mechanism of the catalytic synthesis of water on silver, *Mendeleev Commun.*, 2015, **25**(2), 155–156, DOI: 10.1016/j.mencom.2015.03.028.

74 E. V. Dokuchits, A. V. Khasin and A. A. Khassin, Mechanism and kinetics of hydrogen oxidation on silver, *Russ. Chem. Bull.*, 2012, **61**(12), 2225–2229, DOI: 10.1007/S11172-012-0316-Y.

75 E. J. Marek and E. García-Calvo Conde, Effect of catalyst preparation and storage on chemical looping epoxidation of ethylene, *Chem. Eng. J.*, 2021, **417**, 127981, DOI: 10.1016/j.cej.2020.127981.

76 A. Ruiz Puigdollers, P. Schlexer, S. Tosoni and G. Pacchioni, Increasing Oxide Reducibility: The Role of Metal/Oxide Interfaces in the Formation of Oxygen Vacancies, *ACS Catal.*, 2017, **7**(10), 6493–6513, DOI: 10.1021/acscatal.7b01913.

77 J. Deng, X. Xu, J. Wang, Y. Liao and B. Hong, *In situ* surface Raman spectroscopy studies of oxygen adsorbed on electrolytic silver, *Catal. Lett.*, 1995, **32**(1–2), 159–170, DOI: 10.1007/BF00806111.

78 Y. Wei, H. Wang and K. Li, Ce-Fe-O mixed oxide as oxygen carrier for the direct partial oxidation of methane to syngas, *J. Rare Earths*, 2010, **28**(4), 560–565, DOI: 10.1016/S1002-0721(09)60154-X.

79 Z. Huang, N. Gao, Y. Lin, G. Wei, K. Zhao, A. Zheng, Z. Zhao, H. Yuan and H. Li, Exploring the migration and transformation of lattice oxygen during chemical looping with NiFe2O4 oxygen carrier, *Chem. Eng. J.*, 2022, **429**, 132064, DOI: 10.1016/J.CEJ.2021.132064.

80 Y. Gao, X. Wang, J. Liu, C. Huang, K. Zhao, Z. Zhao, X. Wang and F. Li, A molten carbonate shell modified perovskite redox catalyst for anaerobic oxidative dehydrogenation of ethane, *Sci. Adv.*, 2020, **6**(17), eaaz9339, DOI: 10.1126/sciadv.aaz9339.

81 T. Zambelli, J. V. Barth and J. Wintterlin, Thermal dissociation of chemisorbed oxygen molecules on Ag(110): an investigation by scanning tunnelling microscopy, *J. Phys.: Condens. Matter*, 2002, **14**(16), 4241–4250, DOI: 10.1088/0953-8984/14/16/314.

82 A. Hillary and M. Stoukides, Solid electrolyte aided study of hydrogen oxidation on polycrystalline silver, *J. Catal.*, 1988, **113**(2), 295–306, DOI: 10.1016/0021-9517(88)90258-8.

83 A. R. P. Harrison and E. J. Marek, Selective formation of propan-1-ol from propylene *via* a chemical looping approach, *React. Chem. Eng.*, 2022, **7**, 2534–2549, DOI: 10.1039/D2RE00222A.

84 A. Setiawan, T. Pu, I. E. Wachs and S. Rangarajan, Expanding the Reaction Network of Ethylene Epoxidation on Partially Oxidized Silver Catalysts, *ACS Catal.*, 2024, **14**, 17880–17892, DOI: 10.1021/acscatal.4c04521.

85 X. Wang, Y. Gao, E. Krzystowczyk, S. Iftikhar, J. Dou, R. Cai, H. Wang, C. Ruan, S. Ye and F. Li, High-throughput oxygen chemical potential engineering of perovskite oxides for chemical looping applications, *Energy Environ. Sci.*, 2022, **15**(4), 1512–1528, DOI: 10.1039/D1EE02889H.

86 Z. Sun, C. K. Russell, K. J. Whitty, E. G. Eddings, J. Dai, Y. Zhang, M. Fan and Z. Sun, Chemical looping-based energy transformation *via* lattice oxygen modulated selective oxidation, *Prog. Energy Combust. Sci.*, 2023, **96**, 101045, DOI: 10.1016/J.PECS.2022.101045.

87 A. Joshi, S. Kumar, M. Marx, A. H. Trout, S. Gun, Z. Mohammad, Y. Khalifa and L.-S. Fan, Chemical looping methanol oxidation using supported vanadium phosphorous oxide carriers for formaldehyde production, *J. Mater. Chem. A*, 2024, **12**(13), 7680–7692, DOI: 10.1039/D3TA07468D.

88 G. Mestl, P. Ruiz, B. Delmon and H. Knözinger, *In Situ* Raman Spectroscopy Characterization of 180 Exchange in Physical Mixtures of Antimony Oxides and Molybdenum Oxide The interaction of 1803 with physical mixtures of M0O3 and Sb204 and of M0O3 and, *J. Phys. Chem.*, 1994, **98**, 11283–11292, DOI: 10.1021/j100095a009.

89 A. Stangl, D. Pla, C. Pirovano, O. Chaix-Pluchery, F. Baiutti, F. Chiabrera, A. Tarancón, C. Jiménez, M. Mermoux and M. Burriel, Isotope Exchange Raman Spectroscopy (IERS): A Novel Technique to Probe Physicochemical Processes *In Situ*, *Adv. Mater.*, 2023, **35**(33), 2303259, DOI: 10.1002/ADMA.202303259.